Influence of natural organic matter in the transport medium on fine particle transport

by

© Yuhong Zhou

A Thesis submitted to the

School of Graduate Studies

in partial fulfillment of the requirements for the degree of

Master of Science

Department of Earth Sciences

Memorial University of Newfoundland

December 2017

St. John’s Newfoundland

ABSTRACT

Although extensive research has been conducted to understand the effects of dissolved organic matter (DOM) on fine particle transport, less attention has been paid to NOM in the transport medium (i.e., immobile rock and sediment grains). The objective of this study is to the roles of NOM in the transport medium in mediating particle transport. We conducted an experimental and modelling study on the transport of nanoscale titanium dioxide ($nTiO_2$) and illite colloid in columns packed with quartz sand under water-saturated conditions. Peat moss was used as an example NOM and packed in some of the columns to investigate its influence on particle transport. Experimental results showed that NOM may either increase or decrease particle transport depending on the specific conditions. NOM in the transport medium was found to attract particles and reduce particle mobility when the energy barrier between particle and NOM is low or non-existent. NOM also adsorbed to Fe and Al oxyhydroxides and promoted the transport of negatively-charged particles at low pH. Partial dissolution of NOM releases DOM, and the DOM adsorbs to and increases the transport of positively-charged particles. Additionally, NOM changes pore water pH, which influences particle mobility by affecting the interaction energy between the particle and transport medium. Modelling results showed that the deposition sites of peat moss are very heterogeneous, and the NOM from peat moss may reduce particle deposition rate by adsorbing to the particle and/or transport medium. Findings from this study demonstrates that NOM in the transport medium not only changes properties of the medium, but also may alter water chemistry. Therefore, the role of NOM in mediating particle transport is complicated and dependent on the properties of the particle, NOM, and mineralogical composition of the medium.

ACKNOWLEDGEMENTS

I would first like to give my special thanks to my supervisor, Dr. Tao Cheng, not only for providing the financial support which allowed me to pursue my Master degree abroad, but also for giving me the opportunity meet so many intelligent people during my two years program You supported me greatly and were always willing to help me whenever I met any difficulties. Also, your excellent academic spirit always pushed me to work hard on my research.

In addition, I would like to thank my committee member Titia Praamsma, a senior hydrogeologist at Amec Foster Wheeler, who provided valuable references and advices on my research. Thanks Dr. Valerie Booth for the use of Nano Zetasizer, Jamie Warren for the help of determining dissolved organic carbon in my samples, Pam King for the digestion and ICP-MS measurements, Alison Pye for the help of measuring solid organic carbon, and Wanda Aylward for the help with XRD and SEM measurements.

Also, I must express my gratitude to financial support from the Natural Sciences and Engineering Research Council of Canada (NSERC) Discovery Grant, Canada Foundation of Innovation's Leaders Opportunity Fund and School of Graduate Studies Fellowship provided by Memorial University of Newfoundland.

Finally, I have to express out my appreciation to my family and friends. You always give me energy and power and encourage me to finish my task. Unless your support, I can’t imagine that I can finish my program successfully.

Table of contents

List of Tables

List of Figures

List of abbreviations and symbols

Al – aluminium

Fe – iron

$nTiO_2$ – Titanium dioxide nanoparticles

HA – humic acid

ZP – zeta potential

HDD – hydrodynamic diameter

DOC – dissolve organic carbon

SOC – solid organic carbon

NOM – natural organic matter

DI water – Deionized water

ICP-MS – inductively coupled plasma mass spectrometry

EDX– energy dispersive X-ray

SEM – scanning electron microscope

XRD – X-ray diffraction

cm – centimeter

cm/min – centimeter per minute

cm^3 – cubic centimeter

g – gram

g/cm^3 – grams per cubic centimeter

kg – kilogram

mg – milligram

µg – microgram

µg/L – micrograms per liter

L – liter

ml – milliliter

mg/kg – milligrams per kilogram

mg/L –milligrams per liter

mm – millimeter

mol/L – moles per liter

nm – nanometer

μm – micrometer

Vp– pore volume

pH – power of hydrogen; a measure of hydrogen ion activity

PZC – point of zero charge

BET – specific surface area

DLVO – Derjaguin-Landau-Verwey-Overbeek

LW – London–van der Waals

EDL– electrical double layer

vdW – van der Waals

°C – Degree Celsius

List of Appendices

Chapter 1: Introduction

Natural organic matter (NOM) is ubiquitous in aquatic environments and plays important roles in mediating contaminant transport in groundwater (Aiken et al., 2011; Baalousha, 2009; Dudare and Klavins, 2013; Zhang et al., 2009). NOM contains large number of reactive sites such as carboxylic and phenolic groups, and therefore has high affinity for many solute contaminants including metal ions, radionuclides, and toxic organics (Edgington et al., 2010; Fisher-Power et al., 2016; McCarthy, 1998; McCarthy et al., 1998; Mizutani et al., 2017). When present in the immobile phase of an aquifer (i.e., rocks and sediments), NOM is expected to attract contaminants and reduce their transport. A large amount of NOM exists in the environment as dissolved organic matter (DOM). DOM moves with water flow and competes against binding sites in rocks and sediments for contaminants. As a result, DOM in general mobilizes and facilitates contaminant transport (Cheng and Saiers 2015; Grolimund and Borkovec 2005; Wang et al., 2014 and 2015).

Fine clay particles (e.g., illite colloids) are abundant in subsurface environments and highly mobile under certain geochemical conditions (Cai et al., 2014; Filip and Alberts 1994; Lee et al., 2015; Wang et al., 2014). Previous research has demonstrated that clay colloids have the capacity of adsorbing a variety of contaminants due to their large specific surface area (Flury and Qiu, 2008; Saiers and Hornberger 1999; Turner et al., 2006; Wang et al., 2015). Therefore, when mobile, clay colloids can facilitate the transport of adsorbed contaminants (Flury and Qiu, 2008; Turner et al., 2006; Wang et al.,2015; Zhuang et al.,2003). Engineered nano-materials like nanoscale titanium dioxide (nTiO_2) and zinc oxide (nZnO) are synthesized and used in many products and processes to enhance quality and performance (Bayat et al., 2015; Fang et al., 2009;

Liu et al., 2012; Sun et al., 2015). Similar to clay colloids, engineered nanoparticles may adsorb and influence the transport of solute contaminants (Bradford et al., 2002 and 2004; French et al., 2009; Huber et al., 2000). Additionally, many engineered nano-materials are toxic and potentially detrimental to microbes, plants, and animals (Miller et al., 2012; Sun et al., 2015). Therefore, transport of clay colloids and engineered nanoparticles are of great importance to contaminant migration and water quality.

Extensive research has been conducted on the transport of clay colloids and engineered nano-particles in porous media (Chen et al., 2015; Fang et al., 2009; Liu et al., 2012; Remédios et al., 2012; Saiers and Hornberger 1999; Wang et al., 2015; Zhuang et al., 2003). Interaction energy between a particle and collector (i.e., immobile phase of an aquifer such as rock or sediment grain) is a key factor that controls particle deposition (i.e., immobilization) and transport. DLVO theory has been used to quantify the interaction energy between particle and collector based on experimentally measured zeta potential and particle size (Chen et al., 2012; Wang et al., 2012; Wu and Cheng, 2016). Water chemistry such as pH, ionic strength, and presence of divalent cations, which governs zeta potential and particle size, is found to have major influence on particle transport (Fang et al., 2009; French et al., 2009; Huber et al., 2000). DOM may substantially alter transport by adsorbing to particle and collector, and thus modifying surface properties (e.g., zeta potential) (Aiken et al., 2011; Chen et al., 2012; Franchi and O'Melia 2003; Wang et al., 2012 and 2013). For most cases, DOM adsorption increases particle transport (Ben-Moshe et al., 2010; Chen et al., 2012; Jones and Su, 2012; Jung et al., 2014; Tiller and O'melia 1993). Under certain conditions, however, DOM may reduce particle mobility by neutralizing particle charge and promoting particle deposition (Wu and Cheng 2016).

Although much work has been done to understand the effects of water chemistry on particle transport, less attention has been paid to the influence from the transport medium (i.e., rock and sediment). A large variety of minerals and natural organic matter co-exist in natural sediments, and the effect of each component on particle deposition could be very different. Additionally, natural organic matter and minerals can change water chemistry through geochemical reactions such as protonation, adsorption and dissolution (Fisher-Power et al., 2016; Mizutani et al., 2017; Redman et al., 2002; Wang and Mulligan, 2006). Changes in water chemistry, in turn, may alter particle transport. NOM, Fe and Al oxyhydroxides, and clay minerals are the most active components in soil and sediment that interact with water and change the transport of solute contaminants (Fisher-Power et al., 2016; Mizutani et al., 2017; Shi et al., 2007 and 2013). A number of investigations also demonstrated that Fe oxyhydroxide patches on quartz sand surface have high affinity for and reduce the transport of negatively charged particles at acidic pH (Wang et al., 2012 and 2013; Wu and Cheng, 2016). While a recent study showed that clay mineral (kaolinite) packed in quartz sand columns enhances the transport of nanoscale zero valent iron (nZVI) through increased electrostatic and steric repulsion (Jung et al., 2014), another study reported that clay minerals (illite, kaolinite, and montmorillonite) in limestone porous media hinder the transport of aluminum oxide and titanium dioxide nanoparticles, attributable to straining of particles by the clays at the pore-throat and the morphology of the clays (Bayat et al., 2015). Morphology and surface properties of natural organic matter are very different from those of common minerals in aquifers (e.g., quartz and clay) (O'Kelly and Sivakumar 2014), and the interactions between NOM and water may change water chemistry. Thus, NOM in the immobile phase of an aquifer is expected to influence particle transport in complicated manners. However, at this time, how NOM in the transport medium controls particle transport is largely unknown.

The aim of this study is to investigate the effects of NOM in the transport medium on particle transport and identify the related mechanisms. Particle breakthrough curves in water-saturated laboratory columns packed with quartz-sand were measured. Dried sphagnum peat moss, a common soil conditioner rich in natural organic matter, was used in packing some of the columns so that its influence on water chemistry and particle transport can be determined. Nanoscale titanium dioxide ($nTiO_2$) and illite colloids were selected as examples of engineered nanoparticles and natural clay particles. pH, zeta potential (ZP), and hydrodynamic diameter (HDD) of the column influent and effluent were measured to identify changes in water chemistry and particle property. Derjaguin–Landau–Verwey–Overbeek (DLVO) theory was applied to analyze interaction energy between particle and collector. A mathematical model that accounts for particle advection and dispersion, as well as mass transfer between pore water and transport medium was used to simulate the experimental breakthrough curves. By comparing experimental and modelling results from different columns, mechanisms of how NOM influences particles deposition and transport are proposed.

Chapter 2: Materials and methods

2.1 Experiments

2.1.1 Preparation of materials

Unless stated otherwise, all the chemicals were certified ACS grade and purchased from VWR. Nanopure water, with resistivity >18.2 MΩ × cm and dissolved organic carbon (DOC) concentration <0.02 mg/L, generated by a Barnstead Nanopure Infinity ultrapure water system (Fisher Scientific), was used for preparation of all solutions and particle suspensions.

Quartz sand. Quartz sand (U.S. Silica) was sieved to the size range of 0.425 to 0.600 mm using stainless steel sieves and washed with nanopure water. Particle concentration in the sand-washed water was monitored by measuring light absorbance of the supernatant using a spectrophotometer at a wavelength of 368 nm. The sand was considered "clean" when the absorbance of the supernatant <0.005. The "clean" quartz sand was transferred to an oven, dried for 12 hours at 110 ℃, cooled to room temperature, and stored in clean plastic containers for use in column transport experiments.

Trace quantities of Fe and Al oxyhydroxides may present on quartz sand surface and change fine particle retention and transport (Lenhart and Saiers, 2002). To determine Fe and Al oxyhydroxide concentration of the water washed quartz sand, around 100 mg dry sand was mixed with trace-metal grade concentrated HF and HNO_3 acids (1.25 mL and 0.25 mL respectively) and heated to 100 ℃ on a hot plate for 72 hours. During this time, the samples were ultrasonicated for 1h each of the days. Once completely digested, the solution was diluted, and metal concentrations were measured using an HP 4500 plus ICP-MS (inductively coupled plasma-mass spectrometry). Surface morphology and elemental composition of the quartz sand was characterized by SEM-EDX (scanning electron microscopy with energy-dispersive spectroscopy).

Peat moss. Peat moss (Hoffman 15503, Canadian sphagnum peat moss, 10 quarts, premium grade), a common soil conditioner rich in natural organic matter, was sieved to smaller than 2 mm in size, and placed in an oven at 80 ℃ until dry. The drying process normally took 8 hours, and moisture content of the peat moss was about 8%, determined by the mass difference before and after drying.

To determine pH of the peat moss, 260 mg dry peat moss sample was mixed with 100 mL nanopure water in a 125 mL HDPE bottle, placed on a VWR orbital shaker table (Model 5000), and shaken at a speed of 20 rpm for 16 hours. Supernatant from the bottle was filtered through a 0.45 μm mixed cellulose ester (MCE) filter for pH measurement using an 8302 Bnumd Ross Ultra pH/ATC Triode electrode (Orion).

To determine the grain size distribution, about 30 mg dry peat moss sample was poured into a vibrating feeder to mix with nanopure water, and the sample was automatically diluted before being analyzed with a laser scattering particle size distribution analyzer (LA-950, Horiba Scientific). Organic carbon content of the dry peat moss sample was measured by elemental combustion analysis using a Carlo Erba NA1500 Series II elemental analyzer. SEM-EDX was used to characterize the surface morphology of the peat moss.

nTiO$_2$ particle suspension. Titanium dioxide (TiO_2) powder (Aeroxide™ TiO_2 P25) with TiO_2 content >99.5% was purchased from Fisher Scientific. According to the manufacturer, the specific surface area (BET method) of the powder and the primary particle size of the TiO_2 particle were 35−65 m^2/g and 21 nm respectively. X-ray diffraction (XRD) analysis showed that the powder is a mixture of anatase (90%) and rutile (10%) with particle size of 23 and 40 nm respectively (Wu and Cheng, 2016). $nTiO_2$ particle suspensions were prepared by mixing 20 mg TiO_2 powder with 1000 mL nanopure water. The mixture was sonicated using a Branson Digital Sonifier (Crystal Electronics) for 30 min with 200W power to disperser the particles.

Illite colloid stock suspension. Illite colloid stock suspensions were prepared by mixing 4.0 g illite powder (IMt-2 Illite-Cambrianshale, Clay Mineral Society) with 1000 mL nanopure water. The mixture was sonicated for 30 min with 200W power, and let stand for 16 hours to settle out the larger particles. Illite particles remaining suspended were carefully transferred using a 5mL pipette into a glass storage bottle for characterization and use in column experiments. Particle concentration of the illite colloid stock suspension was determined gravimetrically by filtering 100 mL of the suspension through a 0.1 μm polyethersulfone membrane filter (Pall Life Sciences).

2.1.2. Zeta potential (ZP) and hydrodynamic diameter (HDD) measurement

To determine zeta potential of the quartz sand, nanopure water washed quartz sand was crushed using a laboratory pulverizer (TE250, Angstrom). 4 grams of the crushed sand was mixed with 2000 mL nanopure water in a glass beaker, vigorously stirred, and sonicated for 30 min. The beaker was then placed on a table to stand overnight to let the large particles settle, after which supernatant in the beaker was transferred into 50 mL polypropylene Falcon centrifuge tubes using a 5 mL pipette for zeta potential measurement.

The procedure used for preparing peat moss samples for zeta potential measurement was similar to that for pH measurement, i.e., 260 mg dry peat moss was mixed with 100 mL nanopure water and gently shaken for 16 hours, and the supernatant from the mixture was filtered through 0.45 μm MCEfilter to remove larger particles. The filtrate was collected in 50 mL polypropylene Falcon centrifuge tubes for zeta potential measurement.

To measure the zeta potential and size of the $nTiO_2$ and illite particles, $nTiO_2$ particle suspension was prepared using the procedure described in Section 2.1.1 and illite particle suspension was prepared by diluting illite colloid stock suspension. Concentration of the $nTiO_2$ and the illite particles in the suspension used for zeta potential and particle size measurement were 20 and 50 mg/L respectively, the same as those used in the column transport experiments.

For all the zeta potential and particle size measurement, ionic strength of the background solution was adjusted to 1 mM by adding NaCl, and pH was re-adjusted to 5.0, 7.0 and 9.0 by adding small volumes of 1.0 M and 0.1 M NaOH and/or HCl solutions. These ionic strength and pH were the same as those in the column transport experiments. A zetasizer nano ZS (Malvern) was used for zeta potential and hydrodynamic diameter measurement. For all the samples, zeta potential and hydrodynamic diameter measurements were performed in triplicate.

2.1.3 Column experiments

Twelve column experiments were conducted to measure $nTiO_2$ and illite particle transport in quartz-sand packed columns (Table 1). Dry peat moss (65 and 260 mg per column respectively) was used in packing some of the columns in order to examine how natural organic matter in the transport media influences particle transport. pH of natural groundwater spans a wide range, therefore two influent pH (5 and 9 respectively) were used in our experiments to examine the effects of peat moss at different pH.

A vertically orientated Kontes ChromaFlex chromatography column (length = 15 cm, inner diameter = 2.5 cm, made of borosilicate glass) was used to hold the quartz sand. Porous HDPE plates, with pore size of 20 µm, were fitted on both ends of the column to support the sand. To pack a column, a few milliliters of 1 mM NaCl background solution was slowly poured into the Kontes column, followed by pouring dry quartz sand or sand-peat moss mixture. The amount of the quartz sand and peat moss was small so that the solids were submerged during packing. A small stainless-steel rod was used to stir the sand and peat moss in the column to homogenize the material and remove any trapped air bubbles. The above procedure was repeated until the column was fully packed (i.e., height of the water-saturated medium reached 15 cm). Pore volume, bulk density, and porosity of the column were calculated based on the volume of the solution, and mass of the sand and peat moss used for packing (Table 1).

The packed column was flushed by particle-free 1 mM NaCl background solution for at least 12 hours before 10 pore volumes of $nTiO_2$ or 7 pore volumes of illite particle suspension were injected. A peristaltic pump (Masterflex, ColeParmer) connected to the column base was used to transfer the background solution and particle suspensions into the column. During both flushing and injection of the particle suspensions, pore water flowed upward with a flow rate of 1 mL/minute. $nTiO_2$ particle suspensions were prepared using the method outlined in Section 2.1.1., and illite particle suspensions were made by diluting the illite colloid stock suspension. Ionic strength of the particle suspensions was adjusted to 1 mM using NaCl, and pH was maintained at 5 or 9 by adding small volumes of 1 M and 0.1 M NaOH and HCl solutions. pH and ionic strength of the background solution used to pack and flush the columns was the same as that of the particles suspensions. All the column experiments were conducted in duplicate at room temperature (~22 ℃). Electrical conductivity of the effluent after the flushing, measured by a conductivity probe, was found practically the same as that of the influent, indicating that leaching of ions from the peat moss and quartz sand was negligible. DOC concentration of some effluent samples was determined by an OI Analytical Aurora 1030 TOC analyzer.

Effluent from the top of the column was collected using a CF-2 fraction collector (Spectrum Chromatography), and particle concentration of the effluent was quantified by measuring the light absorbance of the samples, which was converted to particle concentration based on calibration curves (Fig. A1 and A2). Light absorbance of the $nTiO_2$ and illite particle suspensions was measured at wavelength of 368 nm and 290 nm respectively. Effluent pH was monitored during particle injection using a pH electrode. Effluent samples taken at $V/V_0 \approx 5$ (V is cumulative effluent volume, and V_0 is pore volume of the column) were analyzed for zeta potential and particle size.

2.2 Theoretical aspects

2.2.1 Calculation of DLVO interaction energy

Classical Derjaguin-Landau-Verwey-Overbeek (DLVO) theory was used to quantify interaction energies between particle and collector (i.e., sand and peat moss). Total interaction energy was calculated by combining the London-van der Waals energy (Equation 1) and electrostatic energy (Equation 2).

$$\Phi_{LW} = -\left(\frac{AR}{6s}\right)\left[1+\left(\frac{14s}{\lambda}\right)\right]^{-1} \tag{1}$$

$$\Phi_{EDL} = \pi\varepsilon_0\varepsilon_r R\left\{2\psi_c\psi_s \ln\left[\frac{1+\exp(-\kappa s)}{1-\exp(-\kappa s)}\right]+(\psi_c^2+\psi_s^2)\ln\left[1-\exp(-2\kappa s)\right]\right\} \tag{2}$$

where A (J) is Hamaker constant (Hamaker, 1937), R (m) is radius of the particle, s (m) is separation distance, λ (m) is characteristic wavelength of interaction, usually taken as 10^{-7} m, ε_0 (8.85×10^{-12} $C^2J^{-1}m^{-1}$) is permittivity of vacuum, ε_r (80) is relative dielectric constant of the medium, κ (m^{-1}) is reciprocal of Debye length, and $\kappa=2.32\times10^9\ (\Sigma C_i Z_i^2)^{1/2}$, where C_i is the concentration of ion i and Z_i is its valency value, ψ_c (V) is surface potential of the particle, and ψ_s (V) is surface potential of the collector (Elimelech et al., 2013). The use of Equation 1 and 2 assumes that the particles are spherical in shape, and the sand and peat grains are infinite large plates with smooth surface.

Measured zeta potential and hydrodynamic diameter were used to approximate surface potential and diameter of the particles. To quantify the London–van der Waals energy, six Hamaker constants between particle and collector are needed: TiO_2-H_2O-quartz, TiO_2-H_2O-peat, peat covered TiO_2-H_2O-quartz, peat covered TiO_2-H_2O-peat, illite-H_2O-quartz and illite- H_2O-peat. These Hamaker constants were estimated using Equation 3.

$$A_{132} = (\sqrt{A_{11}} - \sqrt{A_{33}})(\sqrt{A_{22}} - \sqrt{A_{33}}) \tag{3}$$

where 1 is particle (nTiO_2/illite), 2 is collector (quartz sand/peat), 3 is water, and the following constants: $A_{TiO2\text{-}TiO2}$ = 15.3×10^{-20} J (Bergström, 1997), $A_{illite\text{-}illite}$ = 8.6 ×10^{-20} J (Médout-Marère 2000), $A_{quartz\text{-}quartz}$ =6.5×10^{-20} J (Tong et al., 2011), $A_{H2O\text{-}H2O}$ = 3.7×10^{-20} J (Tong et al., 2011). Since the peat moss contains mostly natural organic matter, the Hamaker constant of natural organic matter (NOM) (4.85 ×10^{-20} J, Tong et al., 2011) was used for $A_{peat\text{-}peat}$. For nTiO_2 particles covered by NOM (i.e., nTiO_2 with NOM absorbed), we followed the method used by Tong et al. (2011), i.e., the Hamaker constant of peat ($A_{peat\text{-}peat}$), instead of nTiO_2 ($A_{TiO2\text{-}TiO2}$), was used as A_{11} to calculate the Hamaker constant for $A_{peat\ covered\ TiO2\text{-}H2O\text{-}quartz}$ and $A_{peat\ covered\ TiO2\text{-}H2O\text{-}peat}$.

Based on the Hamaker constant of the induvial materials listed above, the calculated $A_{TiO2\text{-}H2O\text{-}quartz}$ = 1.24 ×10^{-20} J, $A_{TiO2\text{-}H2O\text{-}peat}$ = 2.46 ×10^{-20} J, $A_{peat\ covered\ TiO2\text{-}H2O\text{-}quartz}$ = 1.74 ×10^{-21} J, $A_{peat\ covered\ TiO2\text{-}H2O\text{-}peat}$ = 7.77 ×10^{-22} J, $A_{illite\text{-}H2O\text{-}quartz}$ = 6.32×10^{-21} J, $A_{illite\text{-}H2O\text{-}peat}$ = 2.81×10^{-21} J.

2.2.2 Transport modelling

A model that describes colloidal particle transport in porous medium under steady-state flow conditions (Saiers and Hornberger, 1999) was applied to simulate the breakthrough curves of the column experiments. The movement of particles through the columns was simulated by the advection-dispersion equation with a mass transfer term to account for particle transfer between pore water and the transport medium (Equation 4).

$$\frac{\partial(C)}{\partial t} = av\frac{\partial^2 C}{\partial z^2} - v\frac{\partial(C)}{\partial z} - \frac{\rho_b}{n}\frac{\partial S}{\partial t} \qquad (4)$$

where C is particle concentration in water (mg/L), a is dispersivity (cm), v is average linear pore water velocity (cm/hr), ρ_b is bulk density of the transport medium (g/L), n is porosity (m^3/m^3), S is the total concentration of the particles attached to the medium (mg particle per gram of medium), t is time (hr), z is vertical coordinate (cm), taken to be positive in the upward direction.

Particle attachment to the medium was modelled using an irreversibility kinetics process, based on our experimental results showing that the attached particles did not re-mobilize. 1st order kinetic model (Equation 5, N = 1) reasonably simulated all the breakthrough curves except for $nTiO_2$ breakthrough curves of the experiments with peat moss in the transport medium and influent pH = 9 (i.e., Expt. # 5 and 6, Table 1).

$$\frac{\rho_b}{n}\frac{\partial S}{\partial t} = \sum_{i=1}^{N} k_i\left(1 - \frac{S_i}{S_{i,\max}}\right)C \qquad (5)$$

where k_i is particle deposition rate coefficient of type i site (1/hr), S_i is the concentration of the particles attached to type i site (mg particle per gram of medium), $S_{i,\max}$ is density of type i site (mg particle per gram medium). To mimic these breakthrough curves, 2nd order kinetic model (Equation 5, N = 2) was needed. The particle deposition rate coefficients (k_i) and site densities ($S_{i,max}$) were estimated through inversion by minimizing the sum-of-the-squared residuals between modelled and measured particle concentration in the effluent of each breakthrough curve.

Table 1. Physical and chemical conditions of the column transport experiments

Expt. #	Influent $nTiO_2$ (mg/L)	Influent illite (mg/L)	Peat moss in the column (mg)	Influent pH	Average flow velocity[*] (cm/h)	Column pore volume[*] (cm^3)	Porosity[*]	Bulk density[*] (g/cm^3)
1	20		0	5.0	31.09 ± 0.23	28.41± 0.22	0.39 ± 0.00	1.75 ± 0.00
2	20		65	5.0	30.57 ± 0.12	28.89 ± 0.12	0.39 ± 0.00	1.76 ± 0.01
3	20		260	5.0	31.73 ± 1.34	27.86 ± 1.17	0.38 ± 0.02	1.76 ± 0.02
4	20		0	9.0	32.40 ± 0.73	27.26 ± 0.62	0.37 ± 0.01	1.75 ± 0.01
5	20		65	9.0	31.45 ± 0.76	28.09 ± 0.68	0.38 ± 0.01	1.77 ± 0.01
6	20		260	9.0	31.42 ± 1.46	28.14 ± 1.31	0.38 ± 0.02	1.78 ± 0.01
7		50	0	5.0	30.95 ± 1.59	28.58± 1.46	0.39 ± 0.02	1.74 ± 0.00
8		50	65	5.0	31.57 ± 0.60	27.98 ± 0.54	0.38 ± 0.01	1.75 ± 0.00
9		50	260	5.0	31.29 ± 0.30	28.22 ± 0.28	0.38 ± 0.00	1.77 ± 0.02
10		50	0	9.0	31.66 ± 0.57	27.90 ± 0.50	0.38 ± 0.00	1.74 ± 0.02
11		50	65	9.0	31.29 ± 0.07	28.22 ± 0.06	0.38 ± 0.00	1.76 ± 0.01
12		50	260	9.0	31.13 ± 0.60	28.38 ± 0.55	0.39 ± 0.01	1.78 ± 0.01

[*] Data expressed as mean ± standard deviation of replicate measurement.

Chapter 3: Results and Discussions

3.1. pH, grain size, and organic carbon content of the peat moss

pH of the peat moss in 1 mM NaCl solution was around 6.8 ± 0.1. Mean diameter (mode ± standard deviation) of the peat moss grain was around 0.682 ± 0.093 mm (Fig. A3). Organic carbon content was 40± 4.5 %, indicating the peat moss is made consist mainly of organic matter.

3.2. Zeta potential and hydrodynamic diameter

Zeta potential of $nTiO_2$ in 1 mM NaCl solution was highly sensitive to pH change. At pH 5, $nTiO_2$ was positively charged with zeta potential of +23.6 mV, while at pH 9, $nTiO_2$ carried negative charges with zeta potential of -37.8 mV (Fig. 1a). Zeta potential of $nTiO_2$ was found near neutral (-0.5 mV) at pH 7, consistent with previously reported values of point of zero charge of $nTiO_2$ ($pH_{pzc,\ nTiO2}$ = 6.2 to 6.7) (Englehart et al., 2016, Wu and Cheng 2016). Unlike $nTiO_2$, zeta potential of illite and quartz was not sensitive to pH change, i.e., illite and quartz were negatively-charged throughout the pH range of 5 to 9, with zeta potential ranging from -28.3 to -42.3 mV for illite and from -40.6 to -42.1 mV for quartz (Fig. 1a). The negative zeta potential of illite and quartz under our experimental conditions are in agreement with previously reported point of zero charge of illite and quartz ($pH_{pzc,\ illite}$ = 2.5 to 3, $pH_{pzc,\ quartz}$ = 2.0) (Hussain et al., 1996; Kim and Lawler 2005).

Zeta potential of the peat moss was negative throughout the pH range of 5 to 9, and became slightly more negatively at higher pH, i.e., at pH 5, 7, and 9, the zeta potential was -10.1, -15.2 and -13.2 mV respectively (Fig. 1a). Peat moss is rich in natural organic matter such as humic substances, and the negative charge of the peat moss was presumably due to deprotonation of the carboxylic and phenolic groups of the organic matter.

Hydrodynamic diameter (HDD) of the $nTiO_2$ was small at pH 5 and 9 (269 and 264 nm respectively) (Fig. 1b), due to the repulsive electrostatic forces between particles caused by surface charge. At pH 7, hydrodynamic diameter of the $nTiO_2$ was much larger (839 nm), indicating particle aggregation due to reduced electrostatic forces. Size of the illite particles was not very much influenced by pH change, with hydrodynamic diameter ranging from 349 to 411 nm in the pH range of 5 to 9 (Fig. 1b).

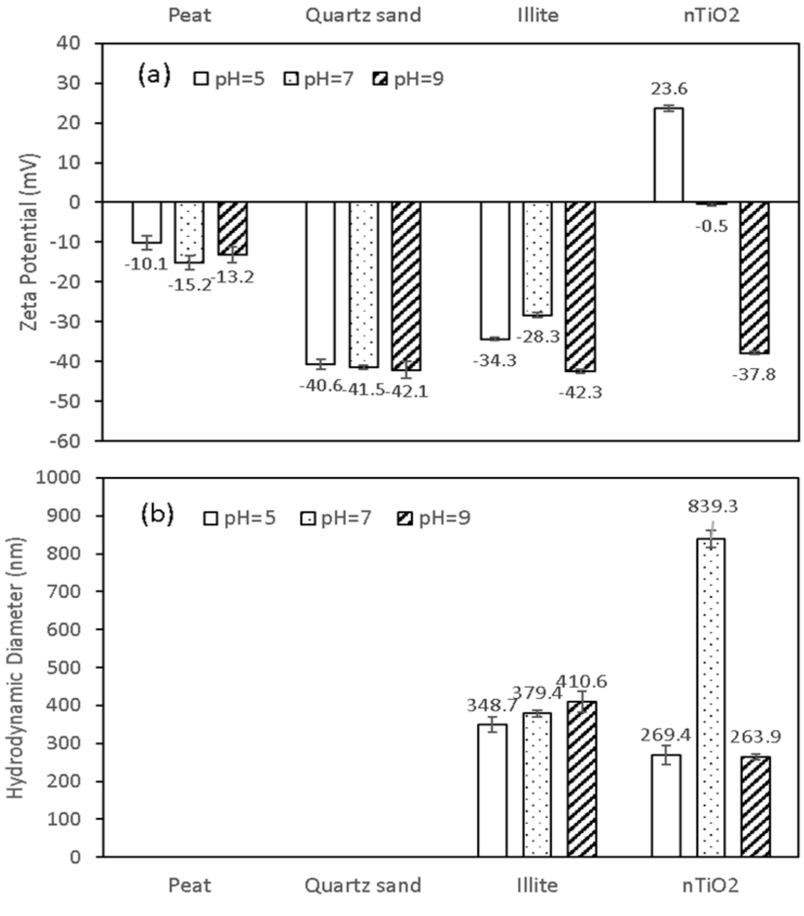

Fig. 1. Zeta potential (ZP) and hydrodynamic diameter (HDD) of peat moss, quartz, illite colloid and $nTiO_2$ in 1 mM NaCl solution at pH 5, 7 and 9. All the hydrodynamic diameter are intensity weighted. Data is expressed as mean ± standard deviation of triplicate measurement.

3.3. Effects of peat moss on particle transport

3.3.1 Effluent pH

In the $nTiO_2$ transport experiments (Expt. #1-6, Table 1), when influent pH = 5.0, effluent pH of the quartz-sand only column (Expt. #1, Table 1) was stable (pH ≈ 5.3) during particle injection and similar to the influent pH (Fig. 2a). For columns with peat moss, effluent pH was also stable but noticeably different from that of the influent, i.e., for the columns with 65 mg and 260 mg peat moss (i.e., Expt. #2 and #3), effluent pH were 6.5 and 7.0 respectively (Fig. 2a), close to the natural pH of peat moss (6.8 ± 0.1). When influent pH = 9.0, effluent pH was different from the influent pH. For the quartz-sand only, 65 mg peat moss, and the 260 mg peat moss column (i.e., Expt. #4-6), effluent pH were 8.2, 7.7, and 7.5 respectively (Fig. 2b).

Similar to the $nTiO_2$ experiments, effluent pH of the illite transport experiments (Expt. #7-12, Table 1) was stable during particle injection but different from the influent pH except for the quartz-sand only column with influent pH = 5.0 (i.e., Expt. #7). When influent pH = 5.0, effluent pH of the quartz-sand only, 65 mg, and 260 mg peat moss column (Expt. #7-9) was 5.1, 5.9 and 6.9 respectively (Fig. 3a). When influent pH = 9.0, effluent pH decreased to 7.6, 7.6, and 7.8 respectively for the quartz-sand only, 65 mg, and 260 mg peat moss columns (Expt. #10-12) (Fig. 3b).

The difference between influent and effluent pH showed that pH of the pore water in the column was buffered by peat and quartz, and the buffering capacity of quartz was relatively weak around pH 5. These results also indicate that pH of pore water in the columns was not uniform, changing from influent pH at the column bottom (influent side) to effluent pH at the column top (effluent side).

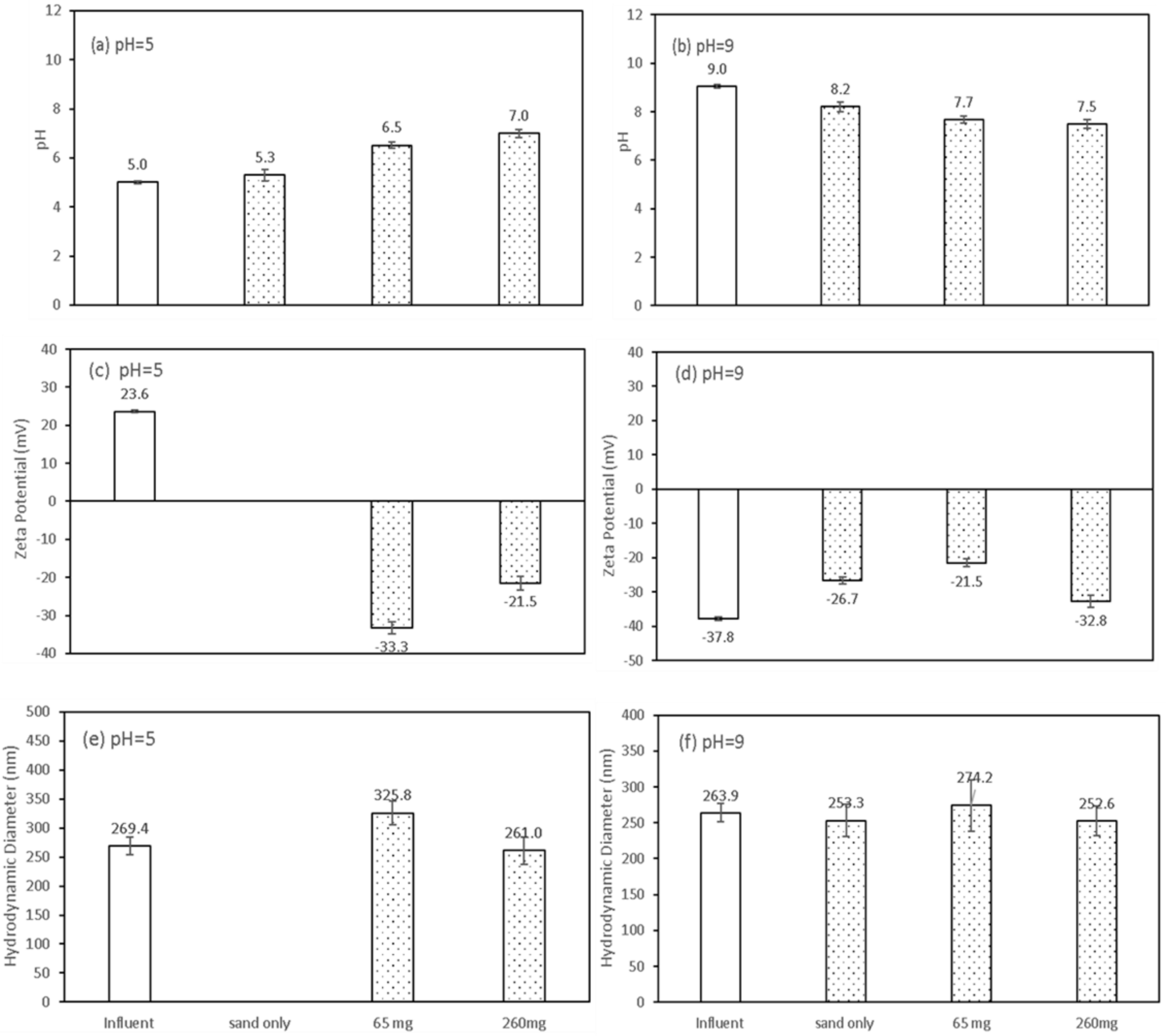

Fig. 2. Influent and effluent pH, zeta potential (ZP), and hydrodynamic diameter (HDD) of the $nTiO_2$ experiments of the quartz-sand only, 65 mg peat moss and 260 mg peat moss columns (empty bars: influent; dotted bars: effluent). Data is expressed as mean ± standard deviation of triplicate measurement. All the hydrodynamic diameter is intensity weighted. Zeta potential and hydrodynamic diameter data were not available for the effluent of the quartz-sand only columns, since no particle was present in the effluent.

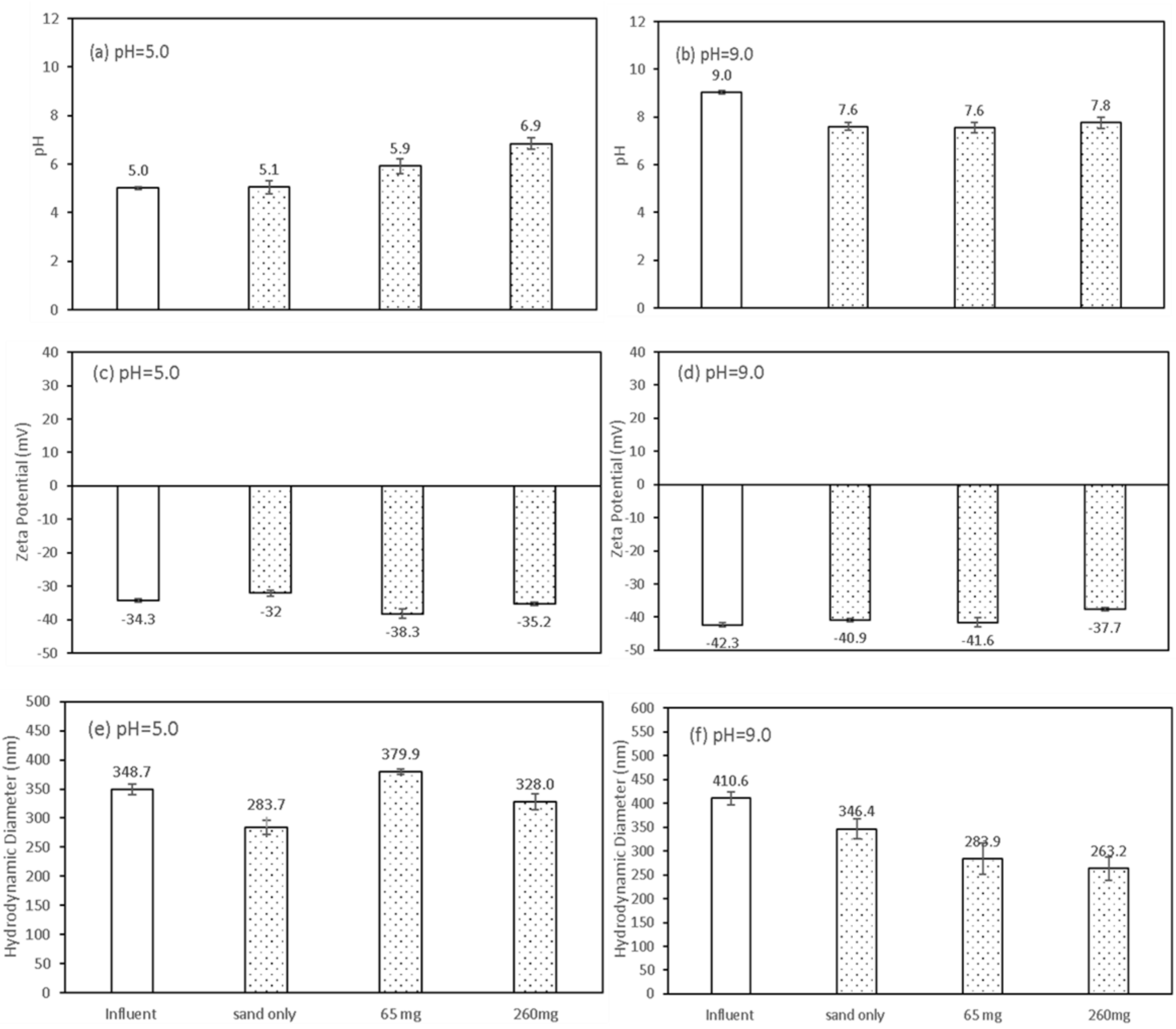

Fig. 3. Influent and effluent pH, zeta potential (ZP), and hydrodynamic diameter (HDD) of the illite colloid experiments of the quartz-sand only, 65 mg peat moss and 260 mg peat moss columns (empty bars: influent; dotted bars: effluent). Data is expressed as mean ± standard deviation of triplicate measurement. All the hydrodynamic diameter is intensity weighted.

3.3.2. $nTiO_2$ transport

Transport of $nTiO_2$ was pH dependent and influenced by the quantity of peat in the column. In all the experiments with influent pH = 5 (Expt. #1-3, Table 1), effluent $nTiO_2$ concentration was low, and peat in the column promoted $nTiO_2$ transport. While no $nTiO_2$ was detected in the effluent of the quartz-sand only column (Fig. 4a), $nTiO_2$ mass recovery in the effluent of the columns with 65 mg and 260 mg peat moss approached 5% and 7% respectively (Table 2). Low mobility of $nTiO_2$ was caused by the attractive electrostatic forces between $nTiO_2$ and the porous medium. Zeta potential of $nTiO_2$, quartz, and peat moss at pH 5 were +23.6, -40.6, and -10.1 mV respectively (Fig. 1a), and the calculated DLVO energy profile showed negative energies between $nTiO_2$ and quartz, and between $nTiO_2$ and peat (Fig. 5a), indicating attractive forces between $nTiO_2$ and the transport medium, and therefore low $nTiO_2$ transport.

The higher $nTiO_2$ transport in columns with peat, in comparison to that in the quartz-sand only column (Fig. 4a) is the result of zeta potential change caused by DOC adsorption to the $nTiO_2$. It is well established that DOC adsorption to colloidal particles and transport media enhances particle mobility via electrostatics and steric effects (Aiken et al., 2011; Chen et al., 2012; Jung et al. 2014; Wu and Cheng, 2016). In the 65 and 260 mg peat moss columns (Expt. #2 and #3), size of the $nTiO_2$ in the effluent (326 to 261 nm) was similar to that in the influent (269 nm) (Fig. 2e). Zeta potential of the effluent, in contrast, was very different from the influent (-33.3 and -21.5 mV vs. +23.6 mV) (Fig. 2c). Although pH of the column effluent increased with respective to that of the influent (pH = 6.5 and 7.0 vs. influent pH 5.0) (Fig. 2a), and such increase may lower the zeta potential, these effluent zeta potentials were much more negative than that in DOC–free 1 mM NaCl solution at similar pH (i.e., ZP_{nTiO2} = -0.5 mV at pH 7.0) (Fig. 1a). In the 65 mg and 260 mg peat moss column experiments, the influent was DOC–free (i.e.,

<0.02 mg/L), but the effluent could contain low concentration DOC (<1 mg/L) based on our preliminary tests, presumably due to partial dissolution of the peat moss. Wu and Cheng (2016) found that DOM, even at low concentrations, change considerably the zeta potential of positively-charged $nTiO_2$ by adsorbing to $nTiO_2$ surface. They reported that for $nTiO_2$ concentration of 20 mg/L, at pH 5 in 1 mM NaCl solution, with humic acid concentration of 0.33 and 0.66 mg DOC/L, zeta potential of $nTiO_2$ were -20.0 and -41.0 mV respectively, substantially lower than that in humic acid–free solution (+24.6 mV). The influent pH and $nTiO_2$ concentration (20 mg/L) in our column experiments are comparable to those in Wu and Cheng's work (2016), therefore, it is expected that DOC could similarly interact with $nTiO_2$ and reverse its zeta potential in our column experiments.

In the columns with peat moss, $nTiO_2$ transport was controlled by two competing processes, i.e., the positively-charged $nTiO_2$ in pore water are attracted to the negatively-charged quartz and peat moss, which removes $nTiO_2$ from water and decreases its mobility. At the same time, DOC adsorbs to $nTiO_2$, changes the zeta potential to negative, and increases $nTiO_2$ transport. The relative importance of these two competing processes depends on factors including concentration and electrical charges of $nTiO_2$ and DOC, kinetics of $nTiO_2$ attachment to the transport medium and DOC adsorption to $nTiO_2$. For the columns with 65 and 260 mg peat moss, only a small amount of $nTiO_2$ (5% and 7% respectively) were recovered in the effluent. This result shows that $nTiO_2$ attachment to the transport medium was the dominant process, which retained over 90% of the injected $nTiO_2$. Nonetheless, a small fraction of $nTiO_2$ gained sufficient negative charges and passed through the column. The DLVO energy profiles calculated based on the zeta potential and hydrodynamic diameter of $nTiO_2$ in the effluent showed large energy barrier between $nTiO_2$ and quartz (64−159 kT), and between $nTiO_2$ and peat (39−57 kT) (Fig. 5e and 5g), which explains the high mobility of these $nTiO_2$ particles.

In the experiments with influent pH = 9 (Expt. #4-6, Table 1), effluent $nTiO_2$ concentration was high, and peat moss in the column inhibited $nTiO_2$ transport. In the quartz-sand only column, almost 90% of the injected $nTiO_2$ was recovered in the effluent, while for the columns with 65 and 260 mg peat moss, $nTiO_2$ recovered in the effluent decreased to 72% and 52% respectively (Fig. 4b and Table 2). The relatively high mobility of $nTiO_2$ in these experiments was caused by repulsive electrostatic forces between $nTiO_2$ and the porous medium. At pH 9, zeta potential of the $nTiO_2$, quartz, and peat moss were all negative (i.e., -37.8, -42.1, and -13.2 mV, respectively) (Fig. 1a), indicating repulsive forces. DLVO calculation confirmed high energy barrier between $nTiO_2$ and quartz (179-233 kT), and between $nTiO_2$ and peat moss (42-87 kT) under both influent and effluent conditions (Fig. 5, right panels), consistent with the high mobility of $nTiO_2$ observed in these experiments.

Substantial amounts of $nTiO_2$ (30-50%) were retained in the columns with peat moss (Expt. # 5 and 6, Fig. 4b and Table 2). This result shows that peat moss in the columns served as a sink for $nTiO_2$, which contradicts the high energy barriers (42-87 kT) indicated by the DLVO calculation. In calculating the interactive energy between $nTiO_2$ and the collector (e.g., quartz or peat), it was assumed that the collector was an infinite large plate with smooth surface. While this assumption is reasonable for the quartz sand (Fig. A4), it neglects the roughness, depressions, protrusions, and the pore structures on the peat moss surface (Fig. A5). Irregularities on collector surface can substantially reduce energy barrier between the particle and collector (Bradford et al. 2002; Martines et al. 2008; Shen et al. 2011), therefore, actual energy barrier between $nTiO_2$ and peat moss is expected to be lower than those calculated. Wu and Cheng (2016) reported $nTiO_2$

attachment to Fe oxyhydroxides at pH = 9, even though calculations based on classic DLVO theory indicated energy barrier and repulsion. Similarly, Bayat et al. (2015) found aluminum oxide and titanium dioxide nanoparticles retained by kaolinite, illite, and montmorillonite in limestone columns under unfavorable deposition conditions. Both Fe oxyhydroxides and clay minerals have unsmooth surfaces and the attachment of fine particles were attributable surface morphology. Our results further showed that natural organic matter such as peat moss may also attract nanoparticles under unfavorable conditions due to surface roughness.

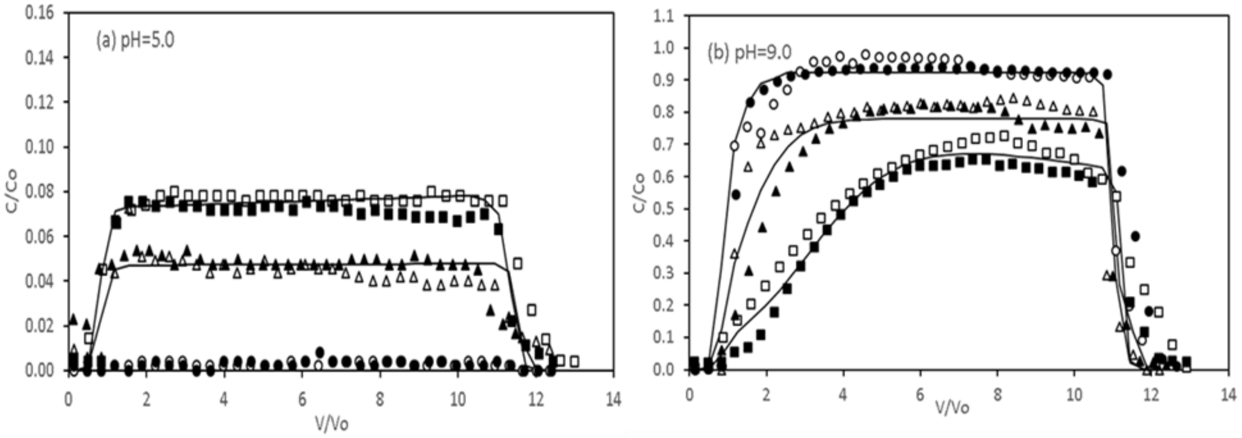

Fig. 4. Experimental (symbols) and modeled (lines) breakthrough curves and effluent mass recovery of $nTiO_2$ (C_0 = 20 mg/L) in quartz sand columns with 0, 65, and 260 mg peat moss (circles: 0 peat moss; triangles: 65 mg peat moss; squares: 260 mg peat moss). Solid and open symbols in panel (a) and (b) represent measurements from duplicate experiments, and lines represent modeled breakthrough curves. 1 mM NaCl solution was used as background electrolyte for all the experiments.

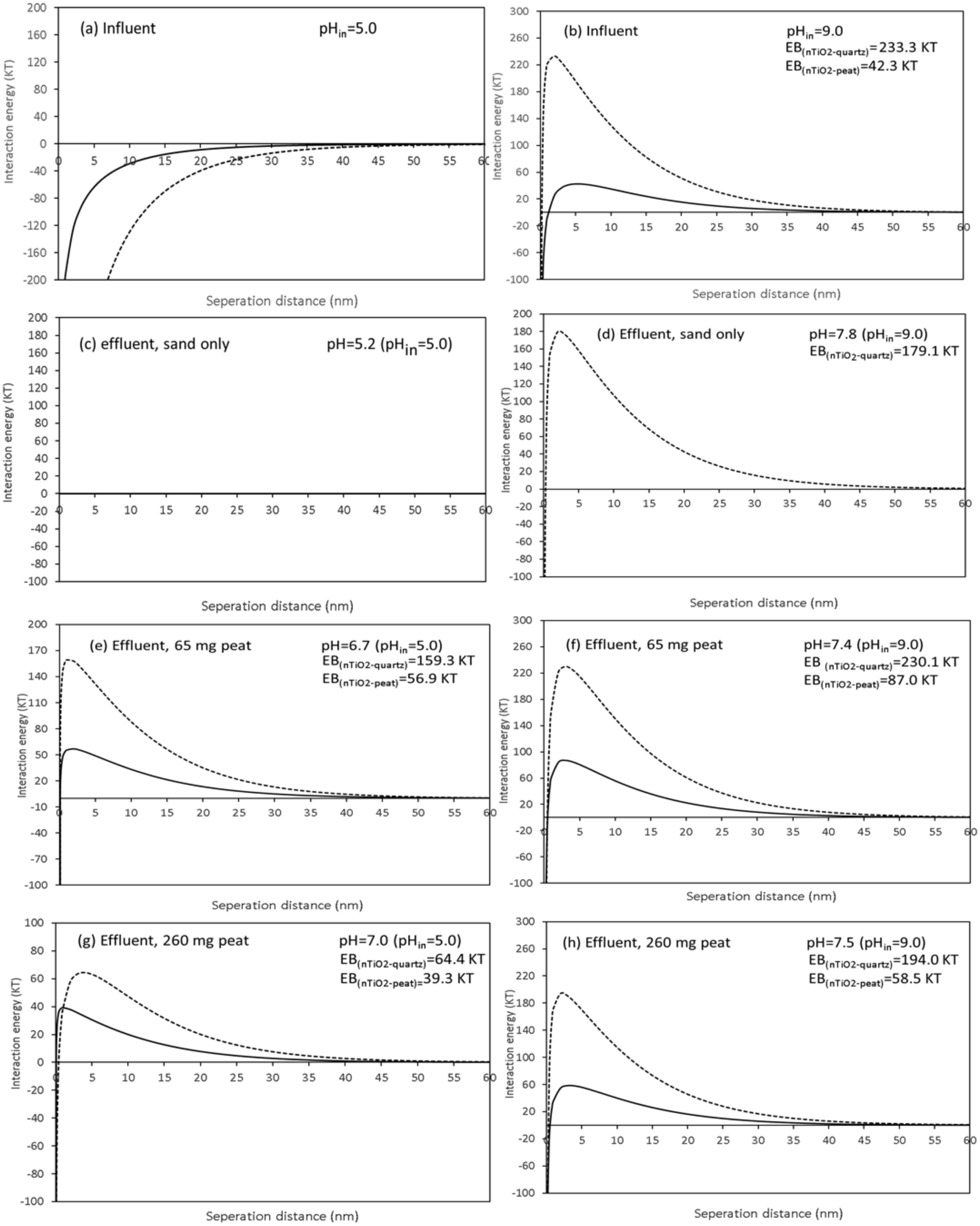
(a) Influent
pH$_{in}$=5.0
(b) Influent
pH$_{in}$=9.0
EB$_{(nTiO2\text{-}quartz)}$=233.3 KT
EB$_{(nTiO2\text{-}peat)}$=42.3 KT
(c) effluent, sand only
pH=5.2 (pH$_{in}$=5.0)
(d) Effluent, sand only
pH=7.8 (pH$_{in}$=9.0)
EB$_{(nTiO2\text{-}quartz)}$=179.1 KT
(e) Effluent, 65 mg peat
pH=6.7 (pH$_{in}$=5.0)
EB$_{(nTiO2\text{-}quartz)}$=159.3 KT
EB$_{(nTiO2\text{-}peat)}$=56.9 KT
(f) Effluent, 65 mg peat
pH=7.4 (pH$_{in}$=9.0)
EB $_{(nTiO2\text{-}quartz)}$=230.1 KT
EB$_{(nTiO2\text{-}peat)}$=87.0 KT
(g) Effluent, 260 mg peat
pH=7.0 (pH$_{in}$=5.0)
EB$_{(nTiO2\text{-}quartz)}$=64.4 KT
EB$_{(nTiO2\text{-}peat)=}$39.3 KT
(h) Effluent, 260 mg peat
pH=7.5 (pH$_{in}$=9.0)
EB$_{(nTiO2\text{-}quartz)}$=194.0 KT
EB$_{(nTiO2\text{-}peat)}$=58.5 KT
Interaction energy (KT)
Seperation distance (nm)
0 5 10 15 20 25 30 35 40 45 50 55 60
200 160 120 80 40 0 -40 -80 -120 -160 -200
300 260 220 180 140 100 60 20 -20 -60 -100
200 180 160 140 120 100 80 60 40 20 0 -20 -40 -60 -80 -100
200 170 140 110 80 50 20 -10 -40 -70 -100
100 80 60 40 20 0 -20 -40 -60 -80 -100

Fig. 5 $nTiO_2$-to-quartz (dashed lines) and $nTiO_2$-to-peat moss (solid lines) DLVO interaction energy profiles in the influent (a, b) and effluent (c, d, e, f, g and h) for experiments with 0, 65, and 260 mg peat moss packed in the column. pH_{in}: influent pH; EB($nTiO_2$-quartz): energy barrier between $nTiO_2$ and quartz; EB($nTiO_2$-peat): energy barrier between $nTiO_2$ and peat moss. Energy profile was not available for the effluent of the quartz-sand only column (panel c), since no particle was present in the effluent.

Table 2. Model calculated particle deposition rate coefficient (k_1 and k_2) and site density ($S_{1, max}$ and $S_{2, max}$) for $nTiO_2$ and illite breakthrough curves.

Expt. #	Peat moss (mg)	Influent pH	Particle mass recovery (%)	k_1 (1/hr)	$S_{1, max}$ (mg/g)	k_2 (1/hr)	$S_{2, max}$ (mg/g)	R^2
1	0	5.0	0.3 ± 0.0	not calculated (no breakthrough)	not calculated (no breakthrough)			
2	65	5.0	5.0 ±0.5	7.53 ± 0.08	1.211 ± 0.908			0.93
3	260	5.0	7.4 ±0.4	6.36± 0.09	1.462 ±1.218			0.91
4	0	9.0	89.3 ± 0.9	0.44 ± 0.12	0.005 ± 0.001			0.94
5	65	9.0	71.6 ± 4.0	2.51 ± 0.00	0.003 ± 0.000	0.56± 0.00	0.001± 0.000	0.97
6	260	9.0	51.9 ± 5.4	5.09 ± 0.60	0.009 ± 0.001	0.58 ± 0.24	0.010 ±0.001	0.95
7	0	5.0	27.2 ±0.8	4.43 ± 0.14	0.152 ± 0.011			0.94
8	65	5.0	54.5 ±7.2	1.36 ± 0.09	0.961 ± 0.301			0.96
9	260	5.0	73.5 ±5.6	0.84 ± 0.11	0.085 ± 0.057			0.93
10	0	9.0	86.5 ± 3.7	0.41 ± 0.09	0.016 ± 0.006			0.97
11	65	9.0	89.4 ± 8.4	0.27 ± 0.00	0.325 ± 6.809			0.94
12	260	9.0	94.8 ± 2.2	0.19 ± 0.05	0.019 ± 0.023			0.98

In the experiments with influent pH = 9 (Expt. #4-6), while size of the $nTiO_2$ in the effluent (253, 274, and 253 nm) was similar to that of the influent (264 nm) (Fig. 2f), zeta potential of the effluent was less negative than that in the influent, i.e., zeta potential of $nTiO_2$ in the influent was -37.8 mV, and effluent zeta potential of the quartz-sand only, 65 mg, and the 260 mg peat moss column were -26.7, -21.5, and -32.8 mV respectively (Fig. 2d). Zeta potentials of the 65 mg and 260 mg peat moss column effluents were close to the zeta potential of the effluent from the quartz-sand only column (-26.7 mV) (Fig. 2d), and were within the range of reported zeta potential of $nTiO_2$ in DOC-free 1 mM NaCl solution at similar pH (-20 to -30 mV at pH ≈ 7.5) (Loosi et al., 2013). These results indicate that the less negative zeta potential of the effluent with respective to that of influent was due to pH decrease (Fig. 2b), instead of the influence from DOC. This is very different from what we observed in the experiments with influent pH = 5 (Expt. #2 and 3), where zeta potential of $nTiO_2$ changed from positive to negative as the water flew through the columns (Fig. 2c). In the experiments with influent pH = 9, pore water pH in the columns ranged from 7.5 to 9.0 (Fig. 2b), higher than the point of zero change of $nTiO_2$ ($pH_{pzc,\ nTiO2} = 6.2-6.7$). Therefore, the $nTiO_2$ particles were negatively-charged and repelled the like-charged DOC. As a result, little DOC should adsorb to the $nTiO_2$. This is consistent with the results of Wu and Cheng (2016), who showed that, at pH 9, humic acid adsorption to $nTiO_2$ is low and humic acid does not influence the zeta potential of $nTiO_2$.

3.3.3 Illite colloid transport

To further understand the effects of peat moss on fine particle transport, we conducted experiments to measure illite colloid transport in columns packed with the same quartz sand and peat moss. In all the experiments, illite recovery in the effluent was higher than that of $nTiO_2$. In the experiments with influent pH = 5, 27% of the injected illite colloids were recovered in the effluent of the quartz-sand only column (Fig. 6a and Table 2), and illite recovery increased to 55% and 74% respectively for the columns with 65 mg and 260 mg peat moss. In the experiments with influent pH = 9, illite recovery were 87%, 89%, and 95% respectively for the quartz-sand only, 65 mg, and 260 mg peat moss columns (Fig. 6b and Table 2).

At pH 5 and 9, illite colloid, quartz, and peat were all negatively charged (Fig. 1a), indicating repulsive electrostatic forces between particle and the transport medium. DLVO energy profiles calculated based on the influent and effluent conditions showed high energy barrier between illite and quartz under all conditions (> 217 kT) (Fig. 7). Energy barriers between illite and peat moss were lower but still substantial, ranging from 24 to 90 kT for the experiments with influent pH = 5 (Fig. 7, left panels), and from 62 to 73 kT for the experiments with influent pH = 9 (Fig. 7, right panels). These calculated energy barriers indicated strong repulsive forces between illite colloid and the transport medium, and explains the high mobility of illite, especially in these experiments with influent pH = 9.

For the quartz-sand only experiment with influent pH = 5, despite the high energy barrier between illite and quartz (>217 kT), only 27% of the injected illite were recovered (Fig. 6a and Table 2). The high particle retention is attributable to illite attachment to Fe/Al oxyhydroxides. The quartz sand used in our experiments was not acid washed, therefore trace quantities of Fe/Al oxyhydroxides could exist as coatings on the sand (Lenhart and Saiers, 2002). This was confirmed by the SEM-EDX results, which detected Fe and Al on sand surface (Appendix 5). Additionally, acid digestion also showed the presence of Fe and Al (107 ± 7 mg Fe/kg sand, and 158 ± 2 mg Al/kg sand). Fe/Al oxyhydroxides, which have high point of zero charge ($pH_{pzc,\ Fe\ oxyhydroxide}$ = 8.7 to 9.1) (Ewbank et al., 2014; Jain et al., 2009; Liu et al., 2005), carry positive charges at pH 5, and are known to increase the retention of negatively-charged colloids and nanoparticles at low pH due to electrostatic attraction (Han et al., 2014; Wu and Cheng, 2016; Wang et al., 2012 and 2013).

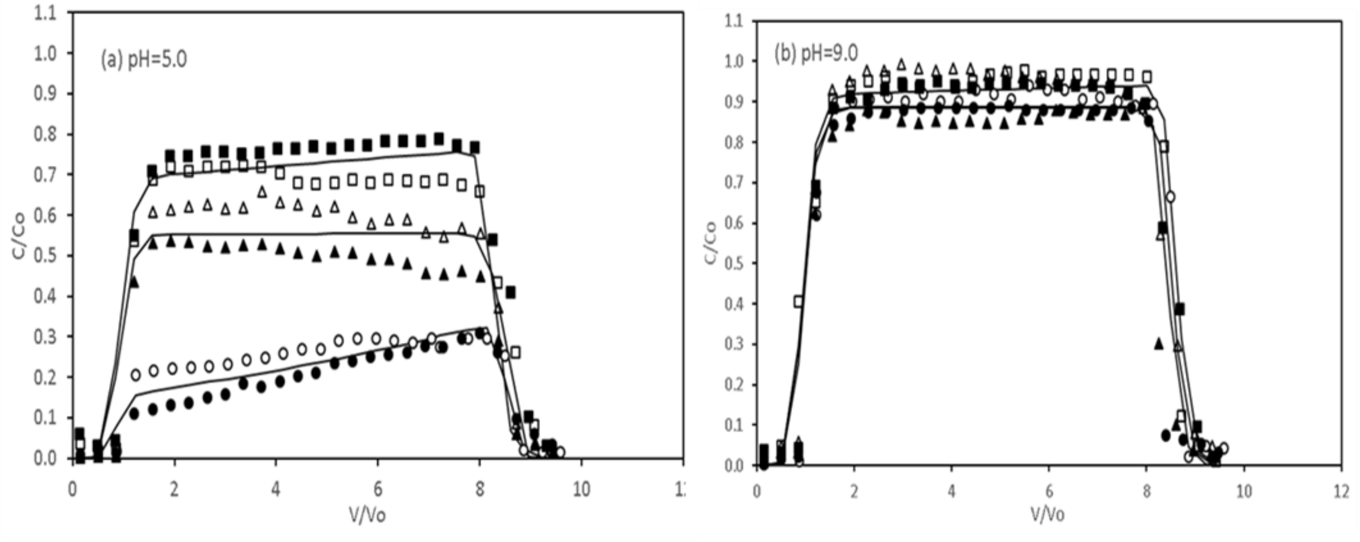

Fig. 6. Experimental (symbols) and modeled (lines) breakthrough curves and effluent mass recovery of illite colloid (C_0 = 50 mg/L) in quartz sand columns with 0, 65, and 260 mg peat moss (circles: 0 peat moss; triangles: 65 mg peat moss; squares: 260 mg peat moss). Solid and open symbols in panel (a) and (b) represent measurements from duplicate experiments, and lines represent modeled breakthrough curves. 1 mM NaCl solution was used as background electrolyte for all the experiments.

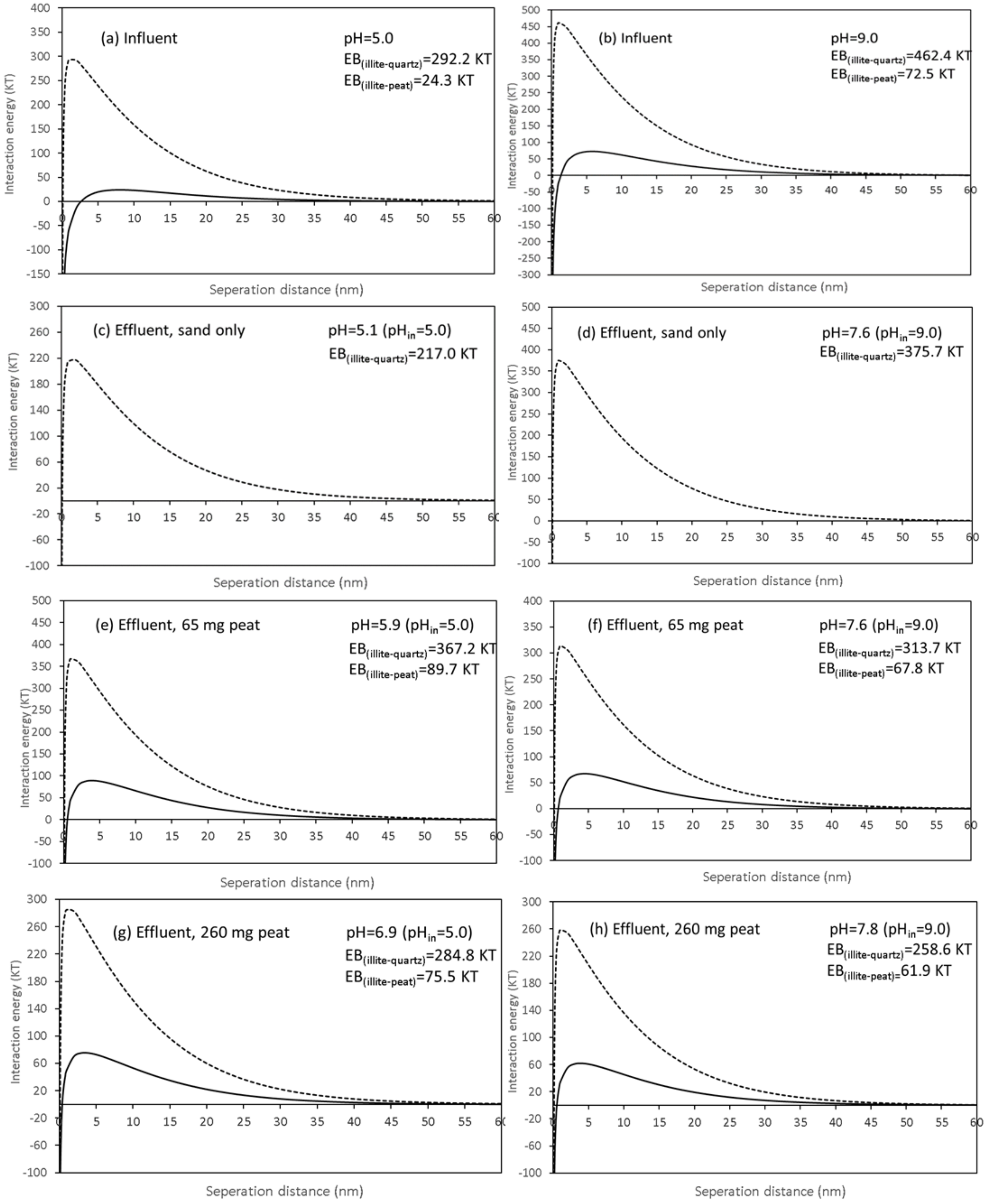
(a) Influent
pH=5.0
EB$_{(illite-quartz)}$=292.2 KT
EB$_{(illite-peat)}$=24.3 KT
(b) Influent
pH=9.0
EB$_{(illite-quartz)}$=462.4 KT
EB$_{(illite-peat)}$=72.5 KT
(c) Effluent, sand only
pH=5.1 (pH$_{in}$=5.0)
EB$_{(illite-quartz)}$=217.0 KT
(d) Effluent, sand only
pH=7.6 (pH$_{in}$=9.0)
EB$_{(illite-quartz)}$=375.7 KT
(e) Effluent, 65 mg peat
pH=5.9 (pH$_{in}$=5.0)
EB$_{(illite-quartz)}$=367.2 KT
EB$_{(illite-peat)}$=89.7 KT
(f) Effluent, 65 mg peat
pH=7.6 (pH$_{in}$=9.0)
EB$_{(illite-quartz)}$=313.7 KT
EB$_{(illite-peat)}$=67.8 KT
(g) Effluent, 260 mg peat
pH=6.9 (pH$_{in}$=5.0)
EB$_{(illite-quartz)}$=284.8 KT
EB$_{(illite-peat)}$=75.5 KT
(h) Effluent, 260 mg peat
pH=7.8 (pH$_{in}$=9.0)
EB$_{(illite-quartz)}$=258.6 KT
EB$_{(illite-peat)=}$61.9 KT
Interaction energy (KT)
Seperation distance (nm)
0
5
10
15
20
25
30
35
40
45
50
55
60

Fig. 7. illite-to-quartz (dashed lines) and illite-to-peat moss (solid lines) DLVO interaction energy profiles in the influent (a, b) and effluent (c, d, e, f, g and h) for experiments with 0, 65, and 260 mg peat packed in the column. pH_{in}: influent pH; EB(illite-quartz): energy barrier between illite colloid and quartz; EB(illite-peat): energy barrier between illite colloid and peat.

In the columns with peat moss, effluent illite recovery was much higher, i.e., illite recovered in the 65 mg and 260 mg peat moss column were 55% and 74% respectively (Fig. 6a and Table 2). As previously discussed, peat moss increased $nTiO_2$ transport at low pH (Fig. 4a) by releasing DOC, which adsorbed to and reversed zeta potential of $nTiO_2$ (Fig. 2c). For the negatively-charged illite colloids, however, DOC is unlikely to adsorb or influence their zeta potential due to electrostatic repulsion. This is evidenced by the similarity in effluent zeta potential of the columns packed with and without peat moss (Fig. 3c and 3d). The higher illite transport in columns with peat moss is presumably caused by organic matter adsorption to the Fe/Al oxyhydroxides. In these experiments, pH of the pore water were 5.9 and 6.9 respectively (Fig. 3a), lower than the pH_{pzc} of Fe/Al oxyhydroxides, indicating positively-charged metal oxyhydroxides, which have high affinity for DOC. Previous studies showed that DOC competes with negatively charged particles for binding sites on Fe oxyhydroxides and promotes particle transport at low pH (Han et al., 2014; Wang et al., 2012 and 2013). In our experiments, organic matter from the peat moss could be attracted to the Fe/Al oxyhydroxides, which masked the positive charges of Fe/Al oxyhydroxides and made them unavailable for illite attachment.

Even with the attachment of organic matter to the Fe/Al oxyhydroxides, a substantial percentage of illite (25-45%) was retained by the transport medium in these experiments (Fig. 6a and Table 2). This is attributable to illite attachment to the peat moss. While the DLVO calculation showed energy barriers between illite and peat moss (24 to 90 kT), as discussed previously, the actual energy barrier should be lower and therefore some of the illite particles could be retained due to surface morphology of the peat moss.

In the experiments with influent pH = 9, illite recovery was higher than that with influent pH = 5, i.e., for influent pH = 9, illite recovery were 87%, 89% and 95% respectively (Table 2). With influent pH = 9, pH of the effluent ranged from 7.6 to 7.8 (Fig. 3b), higher than that for the experiments with influent pH = 5, which ranged from 5.1 to 6.9 (Fig. 3a). The higher pH indicated lower positive charges on Fe/Al oxyhydroxides, and therefore lower attractive forces between illite and the Fe/Al oxyhydroxides, which is consistent with the higher illite recovery observed in these experiments.

3.4 Transport modelling

Modelling results showed that the one-site model worked well for all the breakthrough curves except for $nTiO_2$ breakthrough curves for the experiments with peat moss in the column and influent pH = 9 (i.e., Expt. #5 and #6), where a two-site model was needed (Fig. 4 and 6, Table 2). In the two-site model, $nTiO_2$ attachment was characterized by a slow-kinetic site of higher site density (k_1 and $S_{1,\,max}$) and a fast-kinetic site of lower site density (k_2 and $S_{2,\,max}$). As discussed previously, in Expt. #5 and #6, the main mechanism of $nTiO_2$ retention was particle attachment to the peat moss. For all the other experiments, the main mechanism was particle attachment to quartz or Fe/Al oxyhydroxides. Although in some experiments (e.g., Expt. #2 and #3), peat moss may also contribute to particle retention, due to the much greater mass of quartz and greater attractive forces between particle and quartz, peat moss was expected to play only a minor role. The necessity of two-site model for simulating particle deposition to peat moss suggests that sites of the peat moss were more heterogeneous than those of quartz and Fe/Al oxyhydroxides.

Due to the strong attractive forces between particle and the transport medium, no $nTiO_2$ was detected in the effluent of the quartz sand only column with influent pH = 5 (Expt. #1), therefore no transport modelling exercise was performed (Table 2). $nTiO_2$ breakthrough in the quartz sand only column with influent pH = 9 (Expt. #4) was characterized by single deposition site with very low deposition rate (k_1 =0.44 /hr) and low site density ($S_{1, max}$ = 0.005 mg/g) (Table 2). For all the columns packed with peat moss, the deposition rate coefficient (k_1) and site density ($S_{1, max}$) in the experiments with influent pH = 5 (i.e., Expt. # 2 and 3) were higher than those for the experiments with influent pH = 9 (i.e., Expt. #5 and 6) (Table 2). This is reasonable, since in the pH 5 experiments, the main mechanisms of deposition were attachment of positively-charged $nTiO_2$ to negatively-charged quartz, and therefore there were abundant sites and no energy barrier, resulting in high site density and high deposition rate. While in the pH 9 experiments, the main mechanism of particle retention was $nTiO_2$ attachment to the peat moss, which was much less abundant compared to quartz, and accordingly lower site density. Additionally, $nTiO_2$ and peat moss were like charged, and $nTiO_2$ retention was caused by surface morphology of the peat moss. Therefore, the attractive forces between $nTiO_2$ and the transport medium was low, resulting in low deposition rate. With influent pH = 5, both deposition rate (k_1) and site density ($S_{1, max}$) decreased with increasing peat moss mass (Expt. #2 vs. #3, Table 2). This was caused by DOC adsorption to $nTiO_2$, through which reversed the zeta potential of some $nTiO_2$, resulting in decrease of the overall deposition rate and site density. Conversely, with influent pH = 9, both deposition rate (k_1) and site density ($S_{1, max}$) increased with increasing peat moss mass (Expt. #5 vs. #6, Table 2), which was attributable to the larger amounts of sites provided by the peat moss.

For illite colloid transport, deposition rate coefficient (k_1) and site density ($S_{1, max}$) were also higher for the experiments with influent pH = 5 than those for the experiments with influent pH = 9 (Expt. #7−9 vs. Expt. #10−12, Table 2). As discussed previously, in the pH 9 experiments, as a result of higher pH, the attractive forces between illite and metal oxyhydroxides diminished. The modelling results showed that the decrease in the interactive forces reduced both the rate of deposition (k_1) and site density ($S_{1, max}$).

For both influent pH = 5 or 9, deposition rate (k_1) generally decreased with increasing peat moss mass (Expt. #7−9 and Expt. #10−12, Table 2). Either Expt. #10 or Expt. #11 seemed an outliner, for which the trend reversed. The decrease in deposition rate with increasing peat moss mass was attributable to organic matter adsorption to the Fe/Al oxyhydroxides, which reduced and/or eliminated the positive charges on these metal oxyhydroxides, and therefore decreased the attractive forces between illite and metal oxyhydroxides, resulting in lower deposition rate. However, for either influent pH, no obvious trend could be determined with regard to how the site density varied with the peat moss mass, due to the large uncertainties involved in the calculated site density.

Chapter 4: Summary, conclusions and recommendations

Summary and conclusions

In this study, we used peat moss as a representing NOM and identified a number of mechanisms through which NOM may change $nTiO_2$ and illite particle transport. NOM in the transport medium can attract particles and reduce particle mobility. This happens when the particle and NOM carry opposite charges (e.g., $nTiO_2$ in the experiments with influent pH = 5), or when the energy barrier between particle and solid-phase organic matter is relatively low, in which case the particle may be retained due to surface morphology of the NOM (e.g., $nTiO_2$ in the experiments with influent pH = 9). Under some other conditions, however, NOM may increase particle mobility, e.g., NOM can adsorb to the positively-charged Fe/Al oxyhydroxides and increase the transport of negatively-charged illite colloids. In addition to altering properties of the transport medium, NOM influences particle mobility by changing water chemistry. E.g., NOM may change pore water pH, which influences particle mobility by affecting the interaction energy between particle and the transport medium. Additionally, partial dissolution of NOM releases DOM to water, and the DOM thus generated adsorbs to particles and modifies particle zeta potential. This process was found to reverse the zeta potential of positively-charged particles and increase the transport of such particles (e.g., $nTiO_2$ particles at $pH < pH_{pzc,\ nTiO2}$). However, DOM hardly influences negatively-charged particles due to electrostatic repulsion. Results from modelling of the particle breakthrough curves showed that deposition sites of peat moss are more heterogeneous than those of quartz or Fe/Al oxyhydroxides, and deposition rates are usually higher for particle-to-quartz than those for particle-to-peat moss, due to the stronger attractive forces between particle and quartz. Modelling results also showed that the adsorption of peat moss organic matter to $nTiO_2$ and Fe/Al oxyhydroxides diminishes the attractive forces between particle and collector, and therefore reduces deposition rate. Findings from this study demonstrates that NOM in the transport medium not only changes property of the medium, but also alters water chemistry, both of which could substantially influence fine particle retention and transport in aquifers.

Recommendations for Research

Progress has been made in particle transport by the influence of natural organic matter in the transport medium, but there are many significant research topics and technical support still need remain. The following recommendations are offered for future research in the groundwater contaminant transport.

1. Given the changing of the percentage of solid organic matter (peat moss) and quartz sand, since limited attention has been focused on the effect of the transport medium on particle transport, and surface roughness of solid organic carbon can affect the transport and deposition of nanoparticles and clay colloids in saturated groundwater conditions.
2. The alterative of peat moss as the represent of NOM, which resulting in particles surface coating, surface properties modifications (e.g., zeta potential), aggregation and stabilization, can be selected to further identify the effect of NOM on nanoparticle transport in groundwater system. The major components of NOM, like carbon content, physicochemical characteristics, can be analysed in future studies.
3. To gain more insight into the effects of NOM on particles transport, a range of solution chemistry background conditions, e.g., pH, ionic strength, divalent cations, should be considered. Since background water chemistry, which governs zeta potential and particle size, have major influence on particle transport and deposition.

4. Clay particles (e.g., illite colloids) are abundant in the natural subsurface environments. Based on the review of previous studies, the important groundwater research gap is identified and should be discussed in the future research: how mineral clay and NOM, as the mixer transport media, impact the particles migration.

References

Aiken, G. R., Hsu-Kim, H., Ryan, J. N. 2011. Influence of dissolved organic matter on the environmental fate of metals, nanoparticles, and colloids. Environmental science & technology, 45(8), 3196-3201.

Baalousha, M. 2009. Aggregation and disaggregation of iron oxide nanoparticles: influence of particle concentration, pH and natural organic matter. Science of the total Environment, 407(6), 2093-2101.

Ben-Moshe, T., Dror, I., Berkowitz, B. 2010. Transport of metal oxide nanoparticles in saturated porous media. Chemosphere, 81(3), 387-393.

Bergström, L.1997. Hamaker constants of inorganic materials. Advances in Colloid and Interface Science 70, 125-169.

Bradford, S. A., Yates, S. R., Bettahar, M., Simunek, J. 2002. Physical factors affecting the transport and fate of colloids in saturated porous media. Water Resources Research, 38(12).

Bradford, S. A., Bettahar, M., Simunek, J., Van Genuchten, M. T. 2004. Straining and attachment of colloids in physically heterogeneous porous media. Vadose Zone Journal, 3(2), 384-394.

Bayat, A. E., Junin, R., Mohsin, R., Hokmabadi, M., Shamshirband, S. 2015. Influence of clay particles on Al_2O_3 and TiO_2 nanoparticles transport and retention through limestone porous media: measurements and mechanisms. Journal of Nanoparticle Research, 17(5), 219.

Cai, L., Tong, M., Wang, X., Kim, H. 2014. Influence of clay particles on the transport and retention of titanium dioxide nanoparticles in quartz sand. Environmental science & technology, 48(13), 7323-7332.

Chen, G., Liu, X., Su, C. 2012. Distinct effects of humic acid on transport and retention of TiO_2 rutile nanoparticles in saturated sand columns. Environmental science & technology, 46(13), 7142-7150.

Chen, K. L., Elimelech, M. 2007. Influence of humic acid on the aggregation kinetics of fullerene (C_{60}) nanoparticles in monovalent and divalent electrolyte solutions. Journal of Colloid and Interface Science, 309(1), 126-134.

Chen, M., Xu, N., Cao, X., Zhou, K., Chen, Z., Wang, Y., Liu, C. 2015. Facilitated transport of anatase titanium dioxides nanoparticles in the presence of phosphate in saturated sands. Journal of colloid and interface science, 451, 134-143.

Cheng, T., Saiers, J. E. 2015. Effects of dissolved organic matter on the co-transport of mineral colloids and sorptive contaminants. Journal of contaminant hydrology, 177, 148-157.

Dudare, D., Klavins, M. 2013. Peat humic substances as sorbent for nanomaterials. International Multidisciplinary Scientific GeoConference: SGEM: Surveying Geology & mining Ecology Management, 67.

Dunphy Guzman, K. A., Finnegan, M. P., Banfield, J. F. 2006. Influence of surface potential on aggregation and transport of titania nanoparticles. Environmental Science & Technology, 40(24), 7688-7693.

Edgington, A. J., Roberts, A. P., Taylor, L. M., Alloy, M. M., Reppert, J., Rao, A. M., Klaine, S. J. 2010. The influence of natural organic matter on the toxicity of multiwalled carbon nanotubes. Environmental Toxicology and Chemistry, 29(11), 2511-2518.

Elimelech, M., Gregory, J., Jia, X., Williams, R.A. 2013. Particle Deposition and Aggregation: Measurement, Modelling and Simulation. Butterworth-Heinemann, London.

Englehart, J., Lyon, B. A., Becker, M. D., Wang, Y., Abriola, L. M., Pennell, K. D. 2016. Influence of a polymer sunscreen additive on the transport and retention of titanium dioxide nanoparticles in water-saturated porous media. Environmental Science: Nano, 3(1), 157-168.

Ewbank, J. L., Kovarik, L., Kenvin, C. C., Sievers, C. 2014. Effect of preparation methods on the performance of Co/Al_2O_3 catalysts for dry reforming of methane. Green Chemistry, 16(2), 885-896.

Fang, J., Shan, X. Q., Wen, B., Lin, J. M., Owens, G. 2009. Stability of titanium nanoparticles in soil suspensions and transport in saturated homogeneous soil columns. Environmental pollution, 157(4), 1101-1109.

Federici, G., Shaw, B. J., Handy, R. D. 2007. Toxicity of titanium dioxide nanoparticles to rainbow trout (Oncorhynchus mykiss): Gill injury, oxidative stress, and other physiological effects. Aquatic Toxicology, 84(4), 415-430.

Fisher-Power, L. M., Cheng, T., Rastghalam, Z. S. 2016. Cu and Zn adsorption to a heterogeneous natural sediment: Influence of leached cations and natural organic matter. Chemosphere, 144, 1973-1979.

Filip, Z., Alberts, J. J. 1994. Adsorption and transformation of salt marsh related humic acids by quartz and clay minerals. Science of the total environment, 153(1-2), 141-150.

Flury, M., Qiu, H. 2008. Modeling colloid-facilitated contaminant transport in the vadose zone. Vadose Zone Journal, 7(2), 682-697.

Franchi, A., O'Melia, C. R. 2003. Effects of natural organic matter and solution chemistry on the deposition and re-entrainment of colloids in porous media. Environmental science & technology, 37(6), 1122-1129.

French, R. A., Jacobson, A. R., Kim, B., Isley, S. L., Penn, R. L., Baveye, P. C. 2009. Influence of ionic strength, pH, and cation valence on aggregation kinetics of titanium dioxide nanoparticles. Environmental science & technology, 43(5), 1354-1359.

Grolimund, D., Borkovec, M. 2005. Colloid-facilitated transport of strongly sorbing contaminants in natural porous media: Mathematical modeling and laboratory column experiments. Environmental science & technology, 39(17), 6378-6386.

Han, P., Wang, X., Cai, L., Tong, M., Kim, H. 2014. Transport and retention behaviors of titanium dioxide nanoparticles in iron oxide-coated quartz sand: Effects of pH, ionic strength, and humic acid. Colloids and Surfaces A: Physicochemical and Engineering Aspects, 454, 119-127.

Hamaker, H. C. 1937. The London-van der Waals attraction between spherical particles. Physica, 4(10), 1058-1072.

Huber, N., Baumann, T., Niessner, R.2000. Assessment of colloid filtration in natural porous media by filtration theory. Environmental science & technology, 34(17), 3774-3779.

Hussain, S. A., Demirci, Ş., Özbayoğlu, G. 1996. Zeta potential measurements on three clays from Turkey and effects of clays on coal flotation. Journal of Colloid and Interface Science, 184(2), 535-541.

Jain, A., Sharma, V. K., Mbuya, O. S. 2009. Removal of arsenite by Fe (VI), Fe (VI)/Fe (III), and Fe (VI)/Al (III) salts: Effect of pH and anions. Journal of hazardous materials, 169(1), 339-344.

Jiang, J., Oberdörster, G., Biswas, P. 2009. Characterization of size, surface charge, and agglomeration state of nanoparticle dispersions for toxicological studies. Journal of Nanoparticle Research, 11(1), 77-89.

Jones, E. H., Su, C. 2012. Fate and transport of elemental copper (C_u0) nanoparticles through saturated porous media in the presence of organic materials. Water research, 46(7), 2445-2456.

Jung, B., O'Carroll, D.M., Sleep, B.E., 2014. The influence of humic acid and clay content on the transport of polymer-coated iron nanoparticles through sand. Sci. Total Environ. 496, 155-164.

Kim, J. K., Lawler, D. F. 2005. Characteristics of zeta potential distribution in silica particles. Bulletin of the Korean Chemical Society, 26(7), 1083-1089.

Lee, J., Bartelt-Hunt, S.L., Li, Y., Morton, M., 2015. Effect of 17β-estradiol on stability and mobility of TiO_2 rutile nanoparticles. Sci. Total Environ. 511, 195-202.

Lenhart, J. J., Saiers, J. E. 2002. Transport of silica colloids through unsaturated porous media: Experimental results and model comparisons. Environmental science & technology, 36(4), 769-777.

Liu, H., Wei, Y., Sun, Y., Wei, W. 2005. Dependence of the mechanism of phase transformation of Fe (III) hydroxide on pH. Colloids and Surfaces A: Physicochemical and Engineering Aspects, 252(2), 201-205.

Liu, L., Zhao, H., Andino, J. M., Li, Y. 2012. Photocatalytic CO_2 reduction with H_2O on TiO_2 nanocrystals: Comparison of anatase, rutile, and brookite polymorphs and exploration of surface chemistry. Acs Catalysis, 2(8), 1817-1828.

Loosli, F., Le Coustumer, P., Stoll, S. 2013. TiO_2 nanoparticles aggregation and disaggregation in presence of alginate and Suwannee River humic acids. pH and concentration effects on nanoparticle stability. Water research, 47(16), 6052-6063.

Martines, E., Csaderova, L., Morgan, H., Curtis, A. S. G., Riehle, M. O. 2008. DLVO interaction energy between a sphere and a nano-patterned plate. Colloids and Surfaces A: Physicochemical and Engineering Aspects, 318(1), 45-52.

McCarthy, J. F. 1998. Colloid-facilitated transport of contaminants in groundwater: mobilization of transuranic radionuclides from disposal trenches by natural organic matter. Physics and Chemistry of the Earth, 23(2), 171-178.

McCarthy, J. F., Czerwinski, K. R., Sanford, W. E., Jardine, P. M., Marsh, J. D.1998. Mobilization of transuranic radionuclides from disposal trenches by natural organic matter. Journal of Contaminant Hydrology, 30(1), 49-77.

Médout-Marère, V. 2000. A simple experimental way of measuring the Hamaker constant A_{11} of divided solids by immersion calorimetry in apolar liquids. Journal of colloid and interface science, 228(2), 434-437.

Miller, R.J., Bennett, S., Keller, A.A., Pease, S., Lenihan, H.S., 2012. TiO_2 nanoparticles are phototoxic to marine phytoplankton. PLoS One 7 (1), e30321.

Mizutani, K., Fisher-Power, L. M., Shi, Z., Cheng, T. 2017. Cu and Zn adsorption to a terrestrial sediment: Influence of solid-to-solution ratio. Chemosphere, 175, 341-349.

O'Kelly, B. C., Sivakumar, V. 2014. Water content determinations for peat and other organic soils using the oven-drying method. Drying Technology, 32(6), 631-643.

Petosa, A. R., Jaisi, D. P., Quevedo, I. R., Elimelech, M., Tufenkji, N. 2010. Aggregation and deposition of engineered nanomaterials in aquatic environments: role of physicochemical interactions. Environmental science & technology, 44(17), 6532-6549.

Petryshyn, R. S., Yaremko, Z. M., Soltys, M. N. 2010. Effects of surfactants and pH of medium on zeta potential and aggregation stability of titanium dioxide suspensions. Colloid journal, 72(4), 517-522.

Redman, A. D., Macalady, D. L., Ahmann, D. 2002. Natural organic matter affects arsenic speciation and sorption onto hematite. Environmental Science & Technology, 36(13), 2889-2896.

Remédios, C., Rosário, F., Bastos, V. 2012. Environmental nanoparticles interactions with plants: morphological, physiological, and genotoxic aspects. Journal of Botany.

Saiers, J. E., Hornberger, G. M. 1999. The influence of ionic strength on the facilitated transport of cesium by kaolinite colloids. Water Resources Research, 35(6), 1713-1727.

Shen, C., Li, B., Wang, C., Huang, Y., Jin, Y. 2011. Surface roughness effect on deposition of nano-and micro-sized colloids in saturated columns at different solution ionic strengths. Vadose Zone Journal, 10(3), 1071-1081.

Shi, Z., Allen, H.E., Di Toro, D.M., Lee, S.Z., Flores Meza, D.M., Lofts, S., 2007. Predicting cadmium adsorption on soils using WHAM VI. Chemosphere 69,605e612.

Shi, Z., Allen, H.E., Di Toro, D.M., Lee, S.Z., Harsh, J.B., 2013. Predicting PbII adsorption on soils: the roles of soil organic matter, cation competition and iron (hydr)oxides. Environ. Chem. 10, 465e474.

Sun, P., Shijirbaatar, A., Fang, J., Owens, G., Lin, D., Zhang, K. 2015. Distinguishable transport behavior of zinc oxide nanoparticles in silica sand and soil columns. Science of the Total Environment, 505, 189-198.

Tiller, C. L., O'Melia, C. R. 1993. Natural organic matter and colloidal stability: models and measurements. Colloids and Surfaces A: Physicochemical and Engineering Aspects, 73, 89-102.

Tong, M., Zhu, P., Jiang, X., Kim, H. 2011. Influence of natural organic matter on the deposition kinetics of extracellular polymeric substances (EPS) on silica. Colloids and Surfaces B: Biointerfaces, 87(1), 151-158.

Turner, N. B., Ryan, J. N., Saiers, J. E. 2006. Effect of desorption kinetics on colloid-facilitated transport of contaminants: Cesium, strontium, and illite colloids. Water resources research, 42(12).

Wang, D., Bradford, S. A., Harvey, R. W., Gao, B., Cang, L., Zhou, D. 2012. Humic acid facilitates the transport of ARS-labeled hydroxyapatite nanoparticles in iron oxyhydroxide-coated sand. Environmental science & technology, 46(5), 2738-2745.

Wang, D., Zhang, W., Zhou, D. 2013. Antagonistic effects of humic acid and iron oxyhydroxide grain-coating on biochar nanoparticle transport in saturated sand. Environmental science & technology, 47(10), 5154-5161.

Wang, S., Mulligan, C. N. 2006. Effect of natural organic matter on arsenic release from soils and sediments into groundwater. Environmental geochemistry and health, 28(3), 197-214.

Wang, Q., Cheng, T., Wu, Y. 2014. Influence of mineral colloids and humic substances on uranium (VI) transport in water-saturated geologic porous media. Journal of contaminant hydrology, 170, 76-85.

Wang, Q., Cheng, T., Wu, Y. 2015. Distinct roles of illite colloid and humic acid in mediating arsenate transport in water-saturated sand columns. Water, Air, & Soil Pollution, 226(5), 129.

Wang, Y., Li, Y., Fortner, J. D., Hughes, J. B., Abriola, L. M., Pennell, K. D. 2008. Transport and retention of nanoscale C_{60} aggregates in water-saturated porous media. Environmental science & technology, 42(10), 3588-3594.

Wang, Y., Gao, B., Morales, V. L., Tian, Y., Wu, L., Gao, J., Yang, L. 2012. Transport of titanium dioxide nanoparticles in saturated porous media under various solution chemistry conditions. Journal of Nanoparticle Research, 14(9), 1095.

Wu, Y., Cheng, T. 2016. Stability of $nTiO_2$ particles and their attachment to sand: Effects of humic acid at different pH. Science of The Total Environment, 541, 579-589.

Xu, S., Gao, B., Saiers, J. E. 2006. Straining of colloidal particles in saturated porous media. Water Resources Research, 42(12).

Xu, S., Saiers, J. E. 2009. Colloid straining within water-saturated porous media: Effects of colloid size nonuniformity. Water resources research, 45(5).

Zhang, Y., Chen, Y., Westerhoff, P., Crittenden, J. 2009. Impact of natural organic matter and divalent cations on the stability of aqueous nanoparticles. Water Research, 43(17), 4249-4257.

Zhuang, J., Flury, M., Jin, Y. 2003.Colloid-facilitated Cs transport through water-saturated Hanford sediment and Ottawa sand. Environmental science & technology, 37(21), 4905-4911.

Appendix 1: Calibration curves of $nTiO_2$ and illite at pH 5 and 9

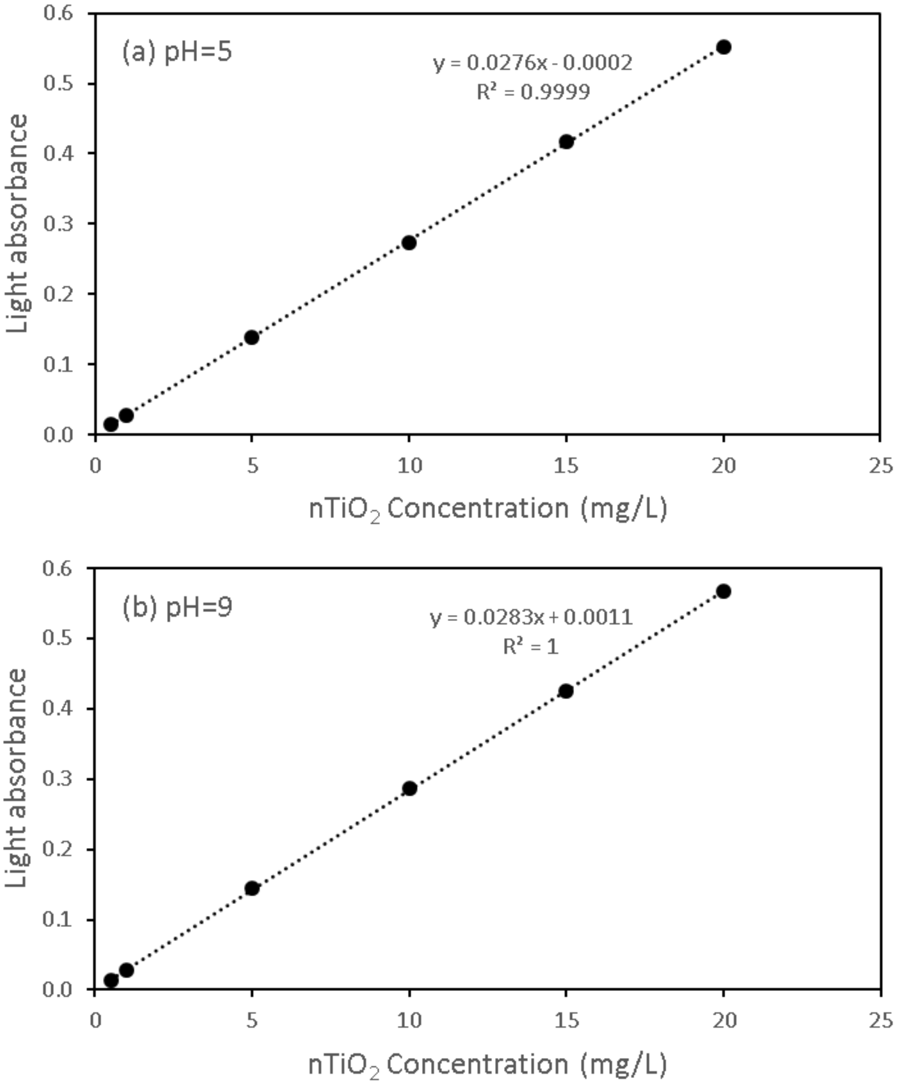

Fig. A1. Calibration curves of $nTiO_2$ at pH 5 (a) and pH 9 (b) in 1 mM NaCl solution. Light absorbance was measured at a wavelength of 368 nm by a spectrophotometer.

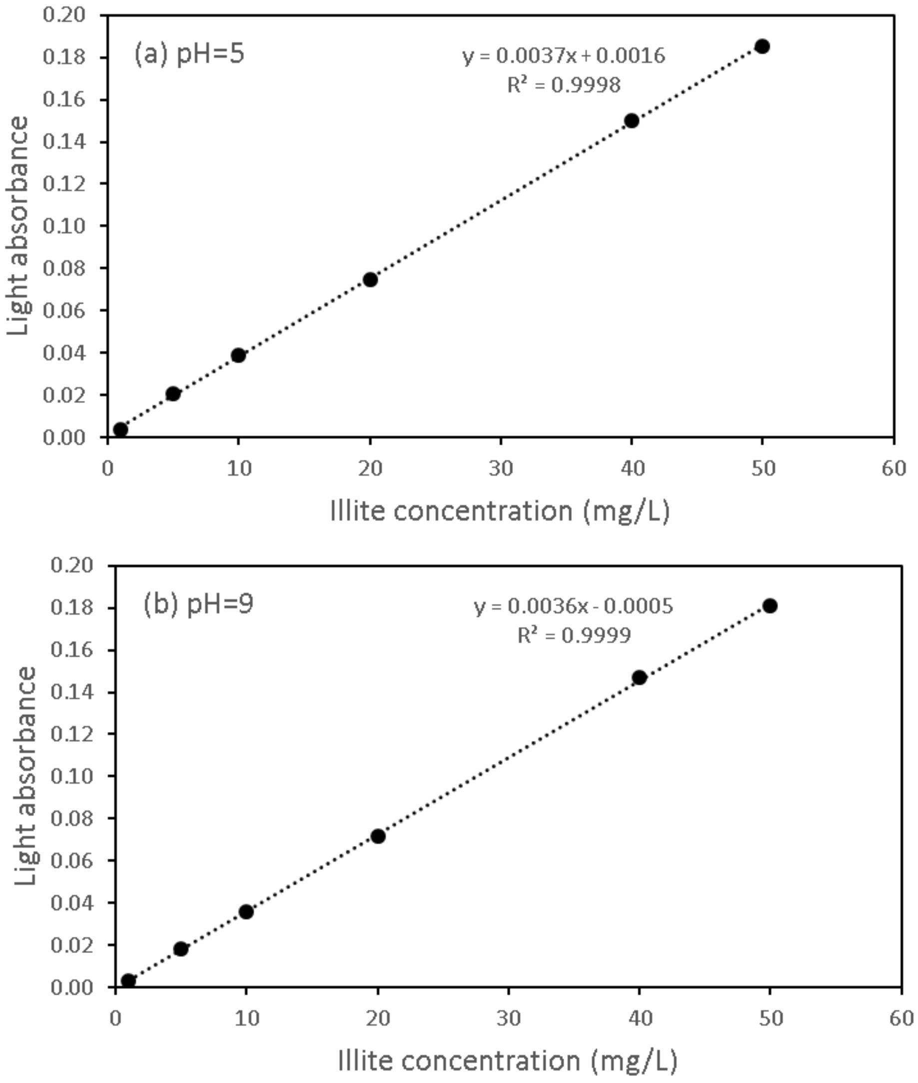

Fig. A2. Calibration curves of illite suspensions at pH 5 (a) and pH 9 (b) in 1 mM NaCl solution. Light absorbance was measured at a wavelength of 290 nm by a spectrophotometer.

Appendix 2: Grain size distribution of the peat moss

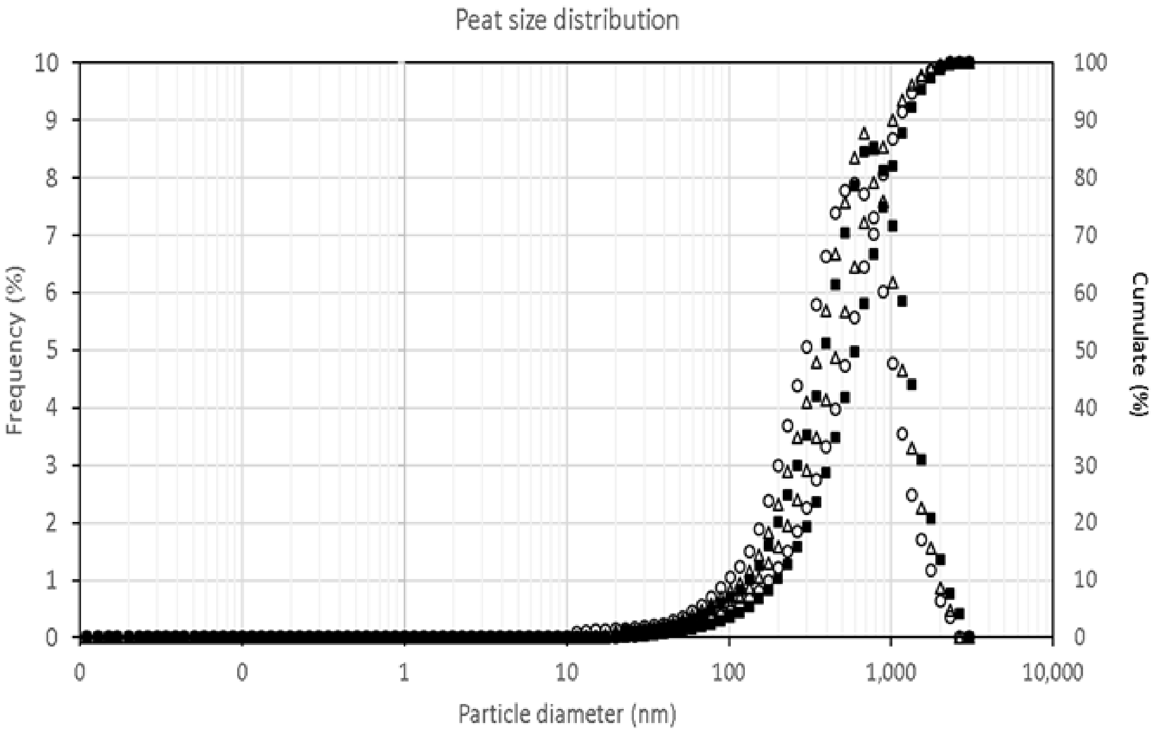

Fig. A3 Grain size distribution of the peat moss. Different symbols represent results from replicate measurements

Appendix 3: SEM of quartz sand

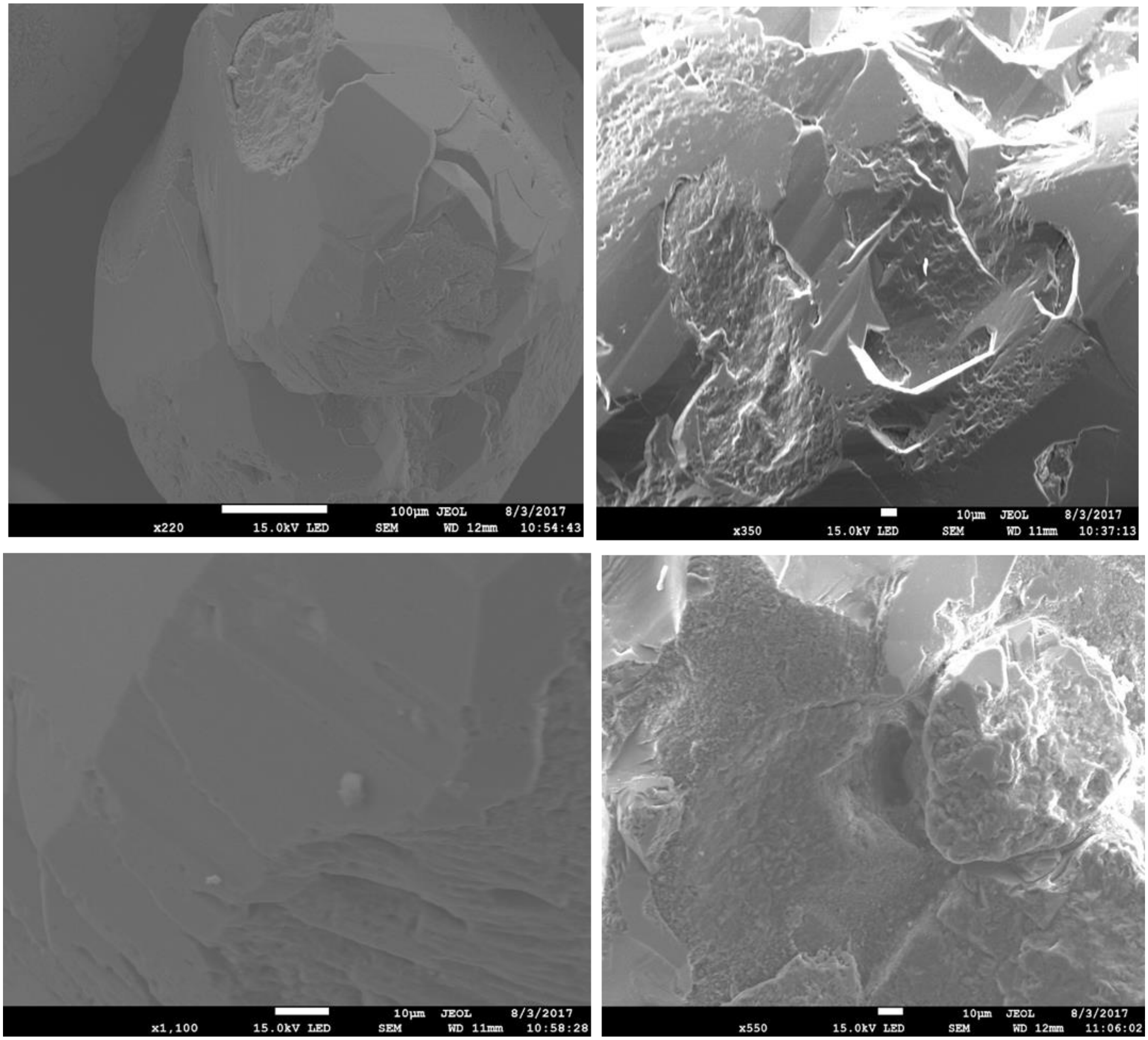

Fig. A4. Representative SEM images of quartz sand

Appendix 4: SEM of peat moss

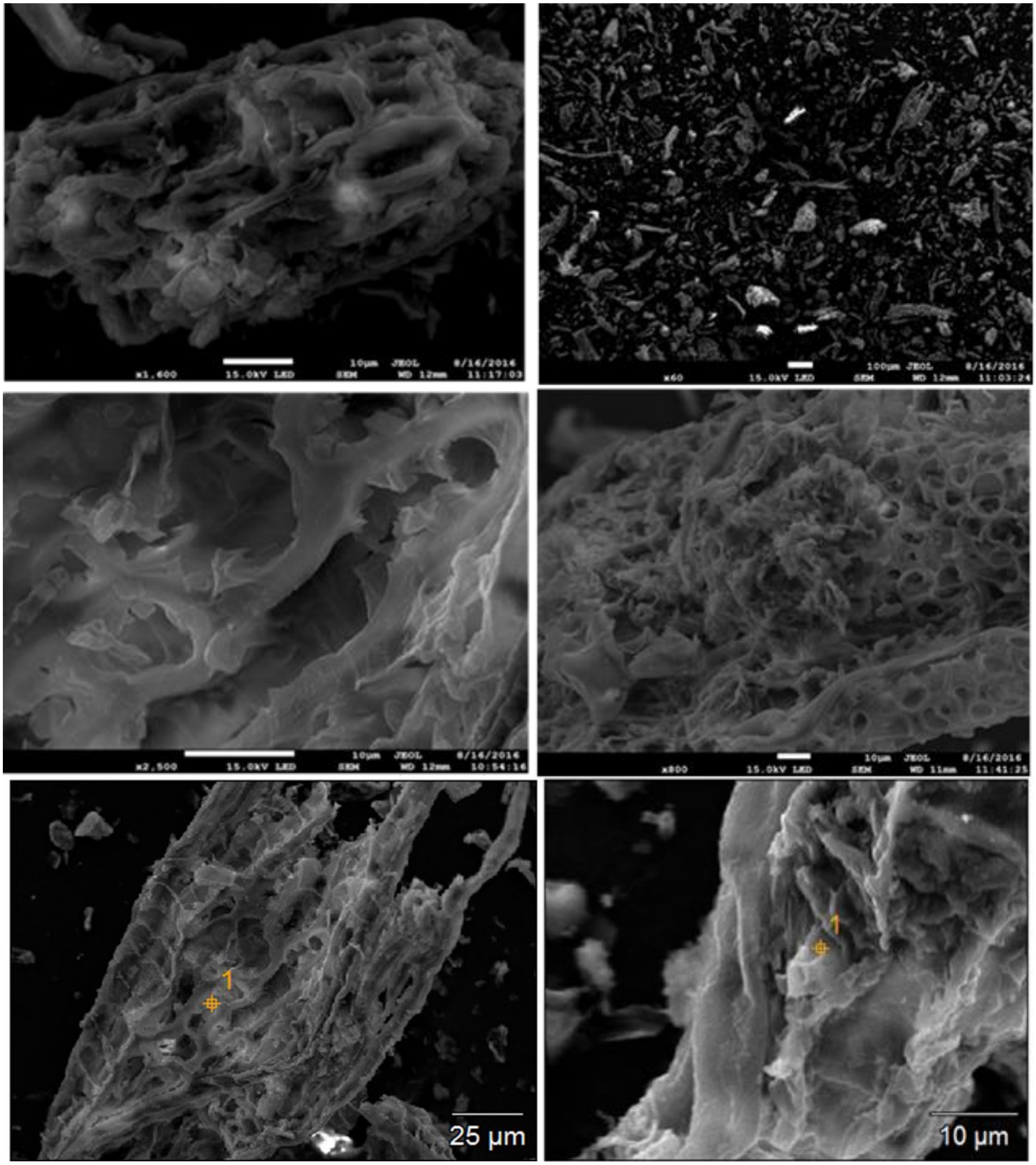

Fig. A5. Representative SEM images of the dry peat moss.

Appendix 5: Energy dispersive X-ray (EDX) spectrum of quartz sand

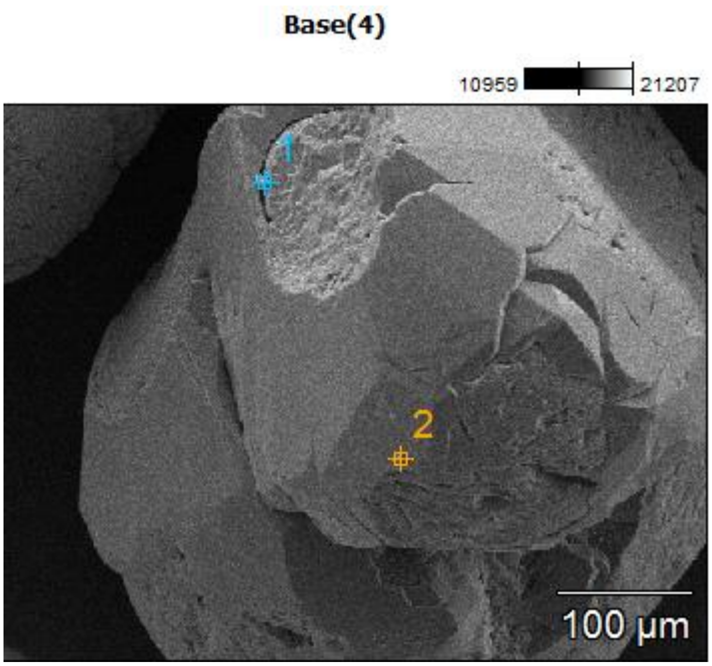

Image Name:	Base(4)
Image Resolution:	512 by 384
Image Pixel Size:	1.08 µm
Acc. Voltage:	15.0 kV
Magnification:	220

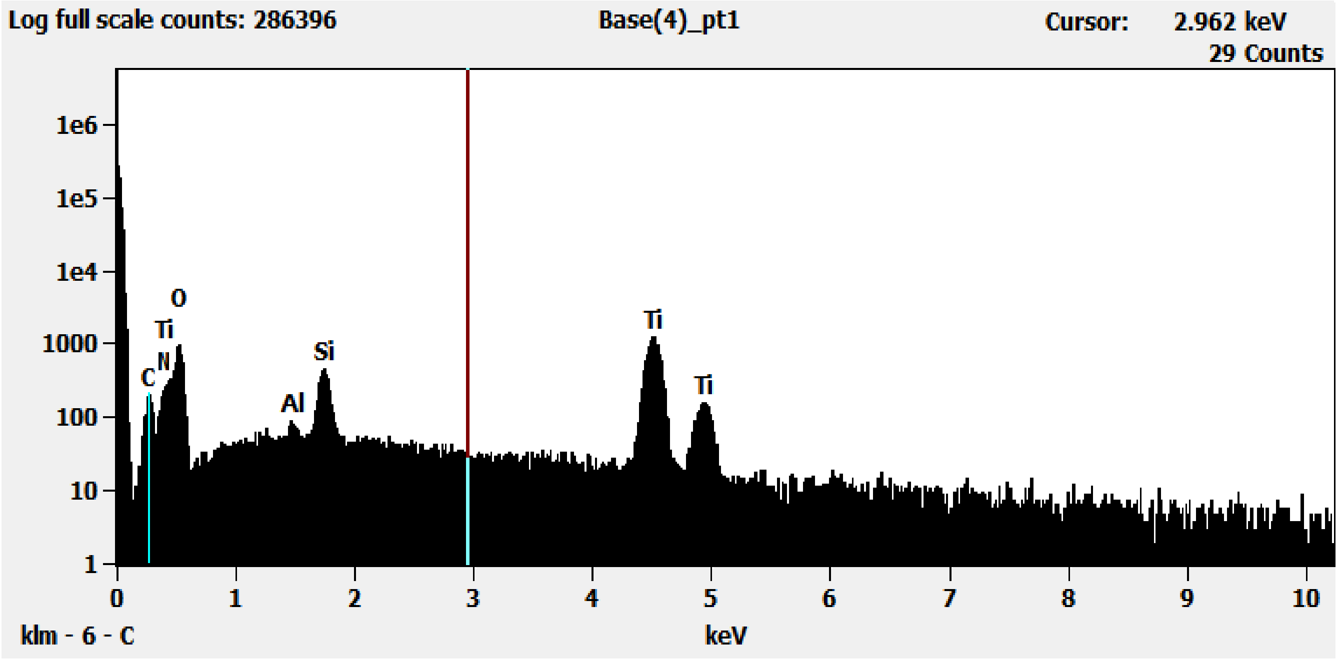

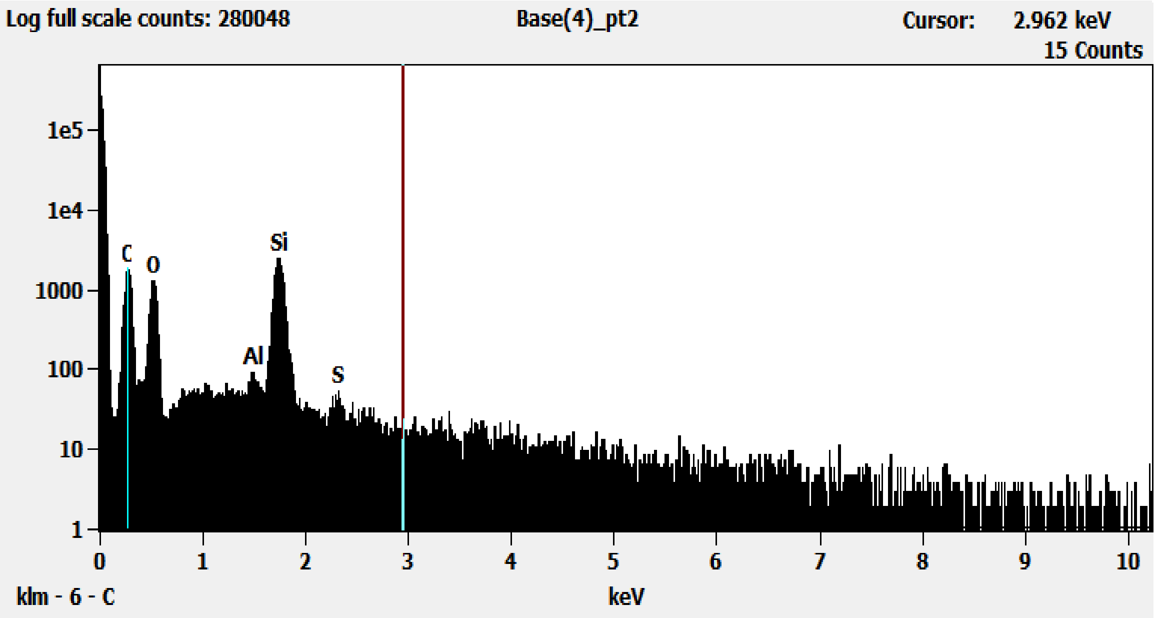
Log full scale counts: 280048
Base(4)_pt2
Cursor: 2.962 keV
15 Counts
1e5
1e4
1000
100
10
1
C
O
Si
Al
S
0
1
2
3
4
5
6
7
8
9
10
klm - 6 - C
keV

Base(7)

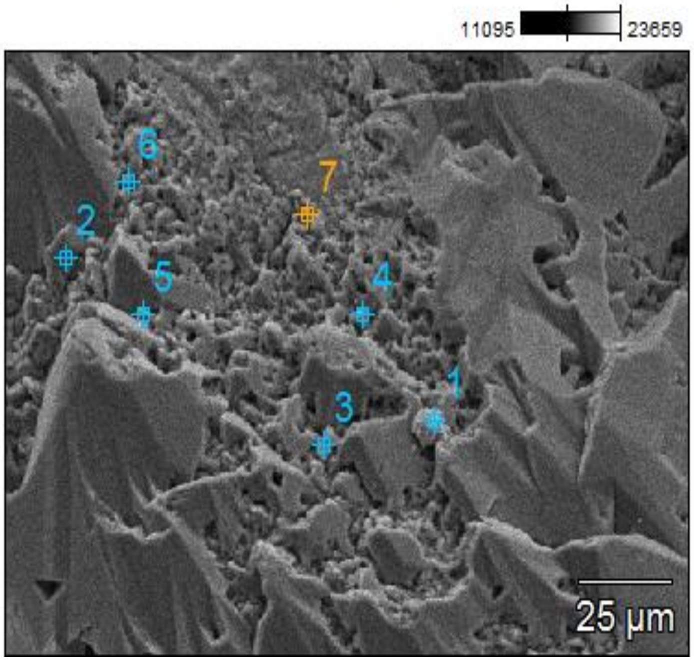

Image Name:	Base(7)
Image Resolution:	512 by 384
Image Pixel Size:	0.36 µm
Acc. Voltage:	15.0 kV
Magnification:	650

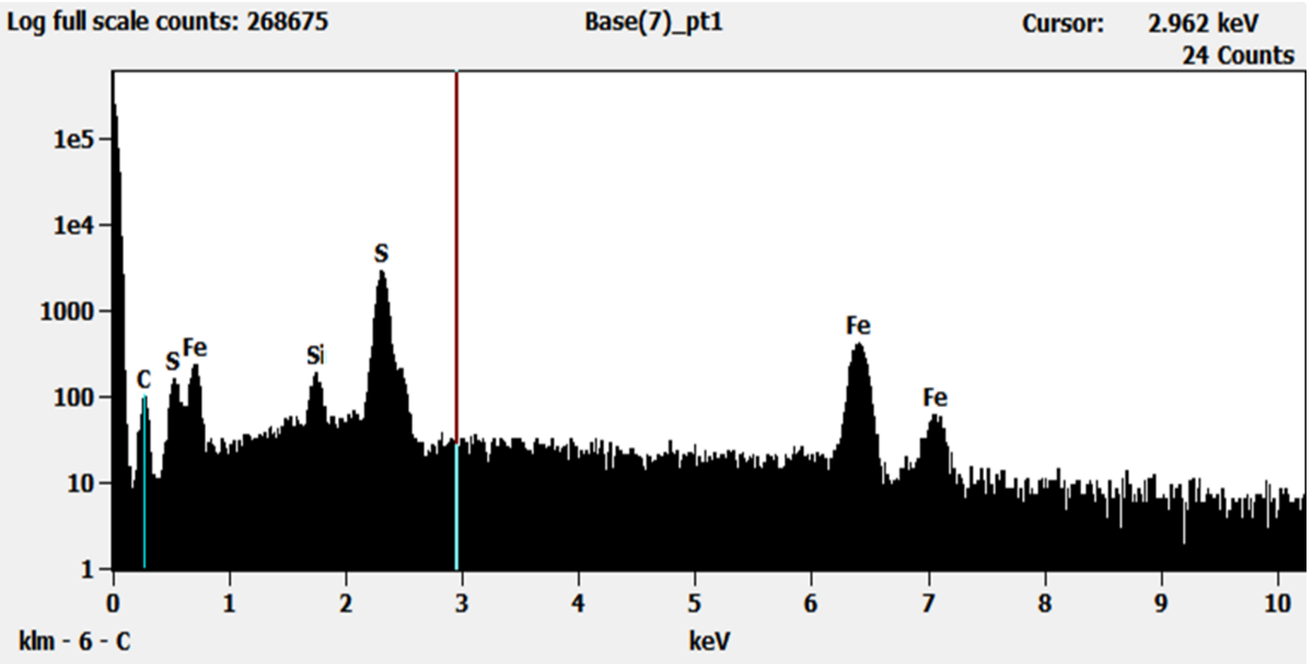

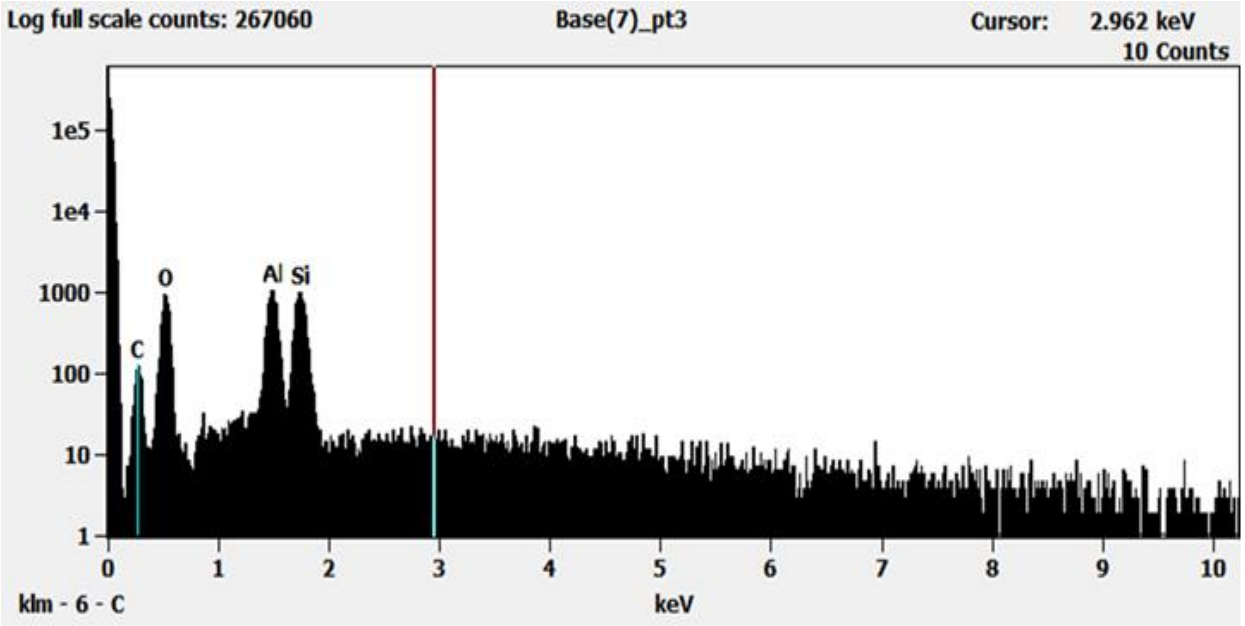
Log full scale counts: 267060
Base(7)_pt3
Cursor: 2.962 keV
10 Counts
1e5
1e4
1000
100
10
1
O
Al
Si
C
0
1
2
3
4
5
6
7
8
9
10
klm - 6 - C
keV

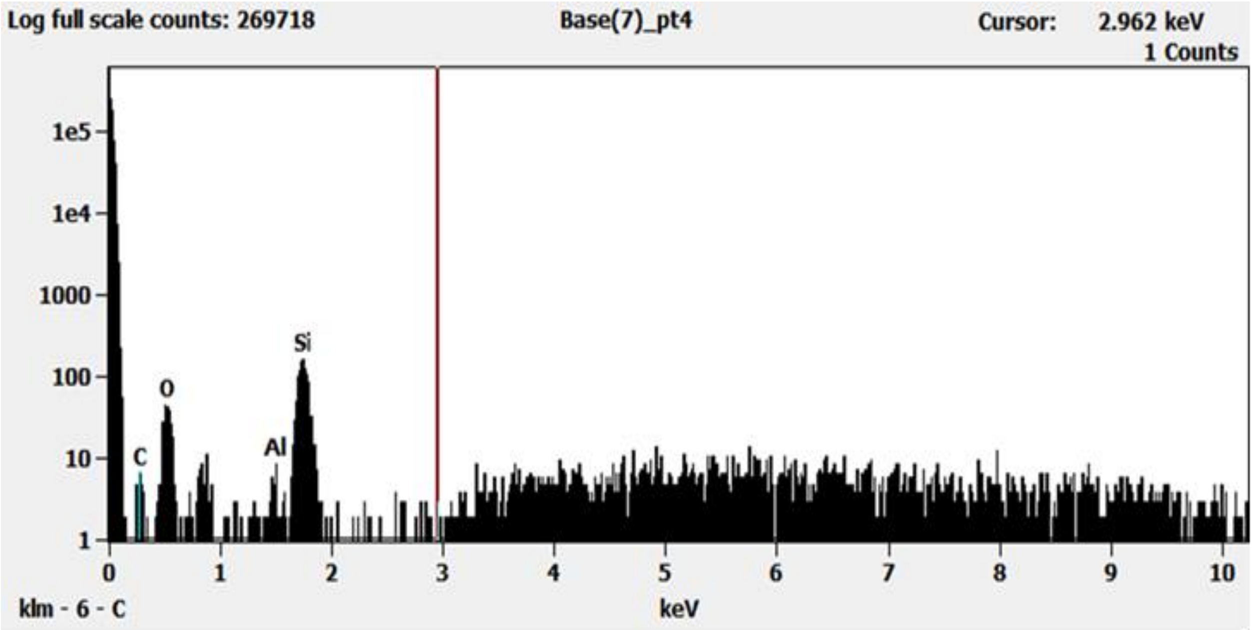
Log full scale counts: 269718
Base(7)_pt4
Cursor: 2.962 keV
1 Counts
1e5
1e4
1000
100
10
1
Si
O
Al
C
0
1
2
3
4
5
6
7
8
9
10
klm - 6 - C
keV

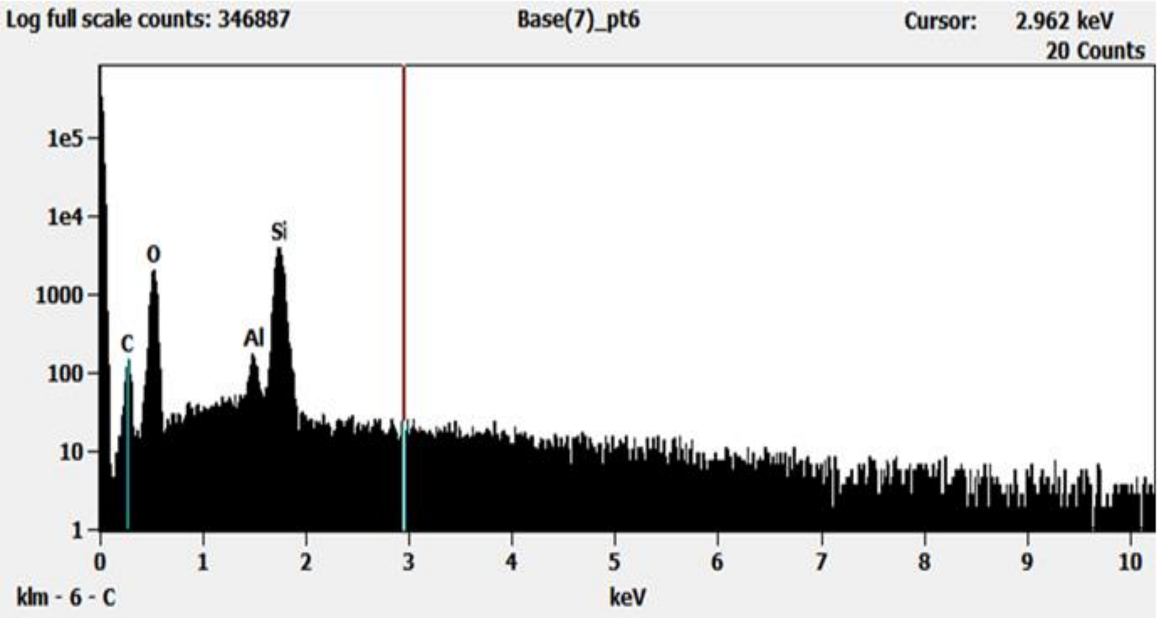
Log full scale counts: 346887
Base(7)_pt6
Cursor: 2.962 keV
20 Counts
1e5
1e4
1000
100
10
1
C
O
Al
Si
0
1
2
3
4
5
6
7
8
9
10
klm - 6 - C
keV

Base(8)

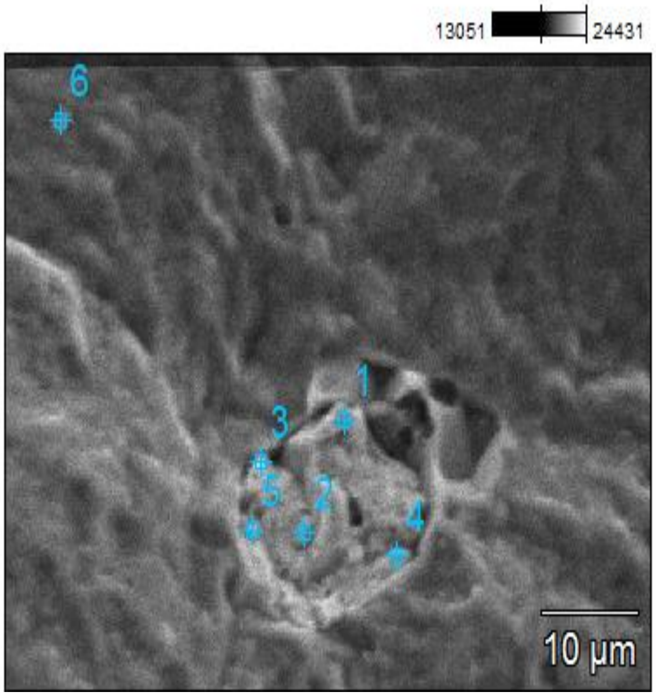

Image Name:	Base(8)
Image Resolution:	512 by 384
Image Pixel Size:	0.13 µm
Acc. Voltage:	15.0 kV
Magnification:	1799

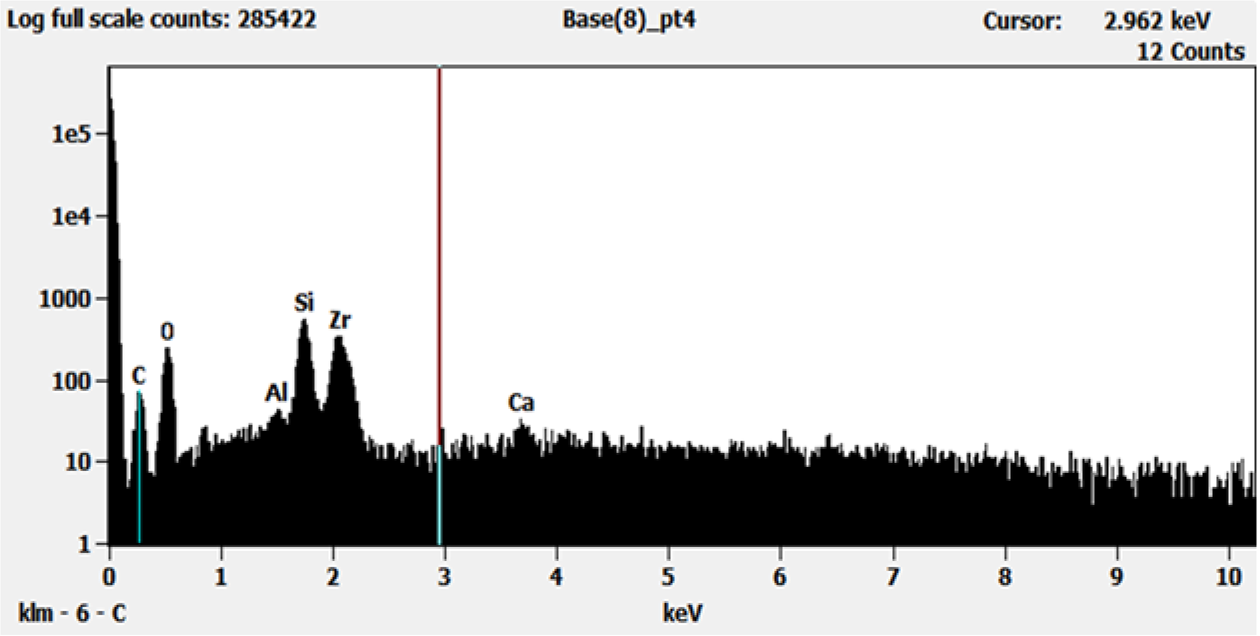

Appendix 6: Energy dispersive X-ray (EDX) spectrum of peat moss

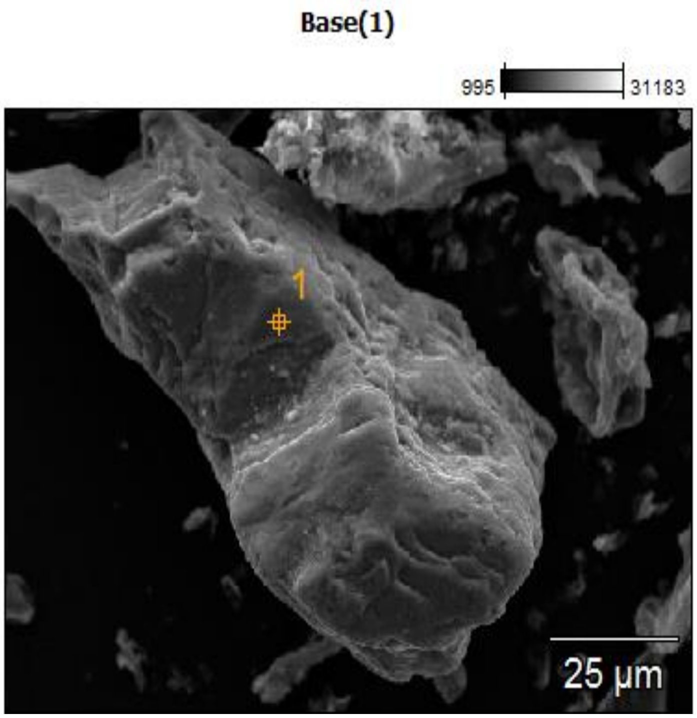

Image Name:	Base(1)
Image Resolution:	512 by 384
Image Pixel Size:	0.26 µm
Acc. Voltage:	15.0 kV
Magnification:	899

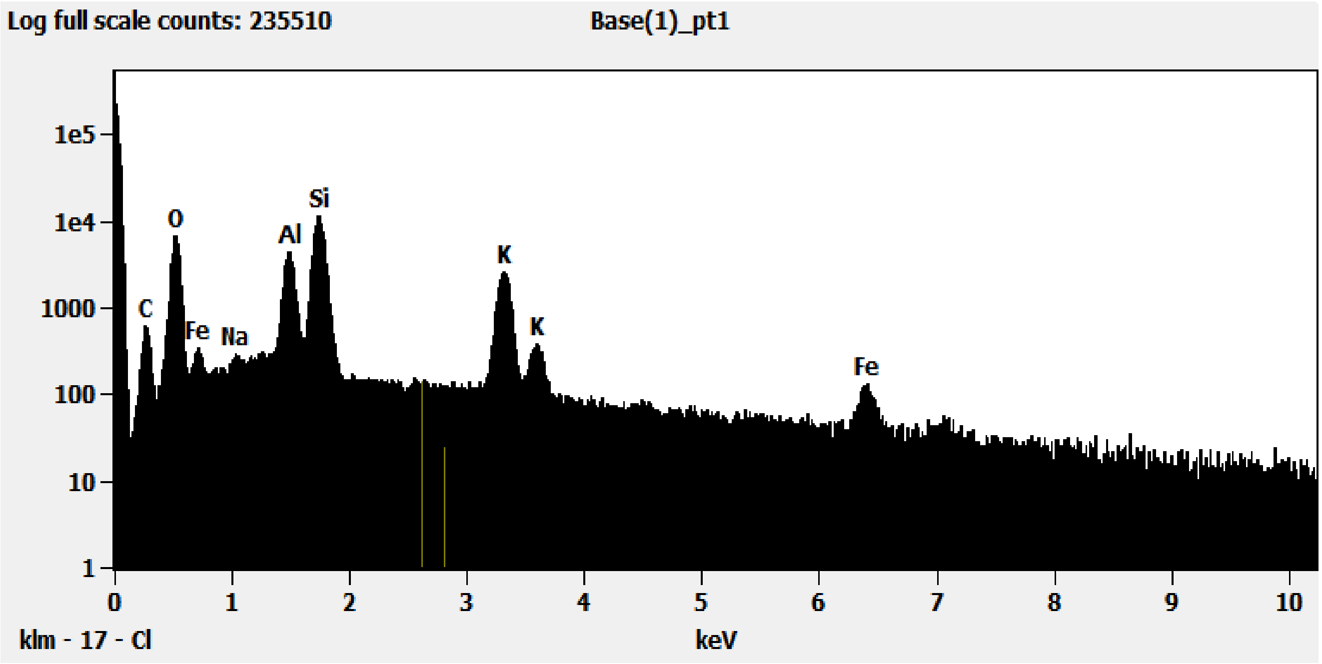

Base(2)

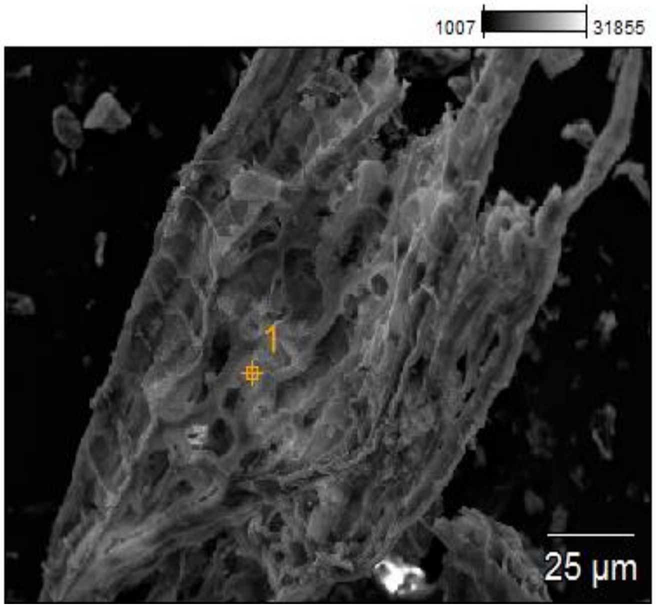

Image Name:	Base(2)
Image Resolution:	512 by 384
Image Pixel Size:	0.36 µm
Acc. Voltage:	15.0 kV
Magnification:	650

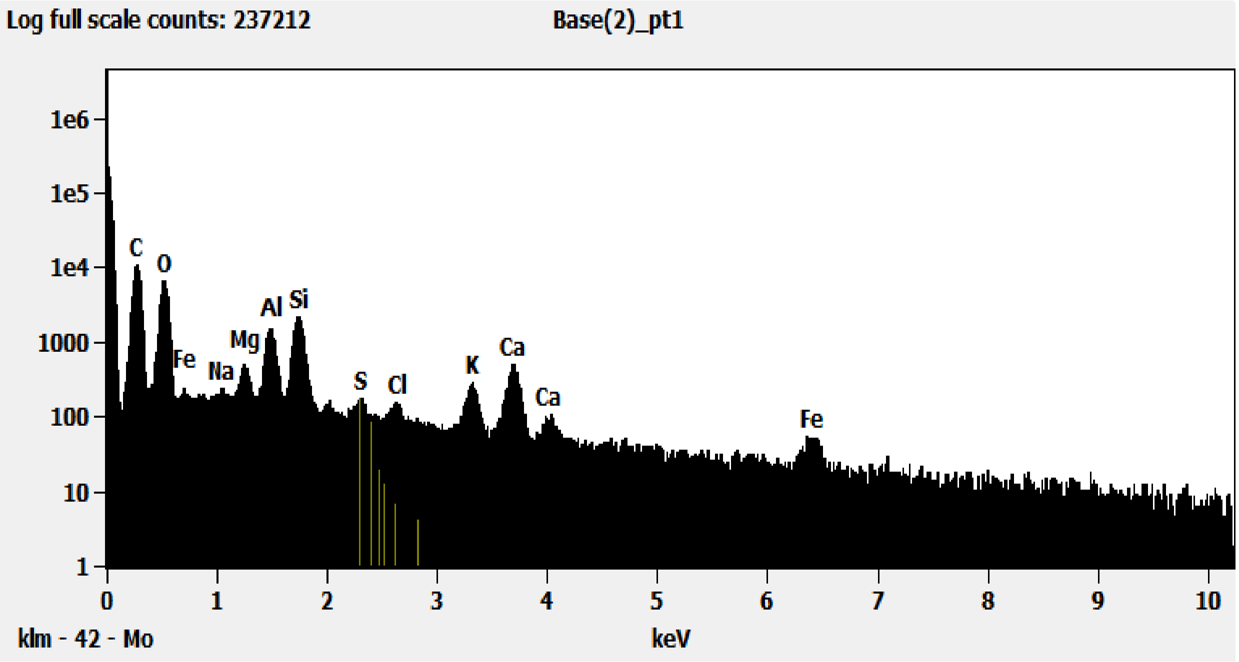

Base(3)

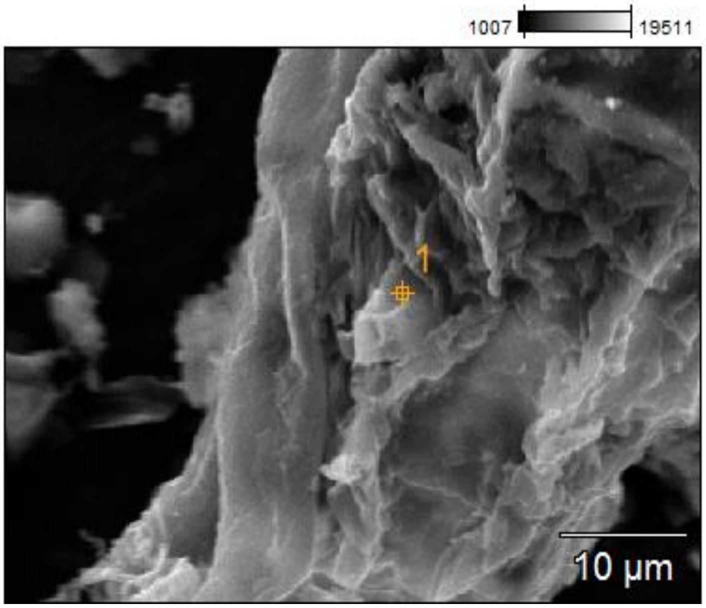

Image Name:	Base(3)
Image Resolution:	512 by 384
Image Pixel Size:	0.11 µm
Acc. Voltage:	15.0 kV
Magnification:	2200

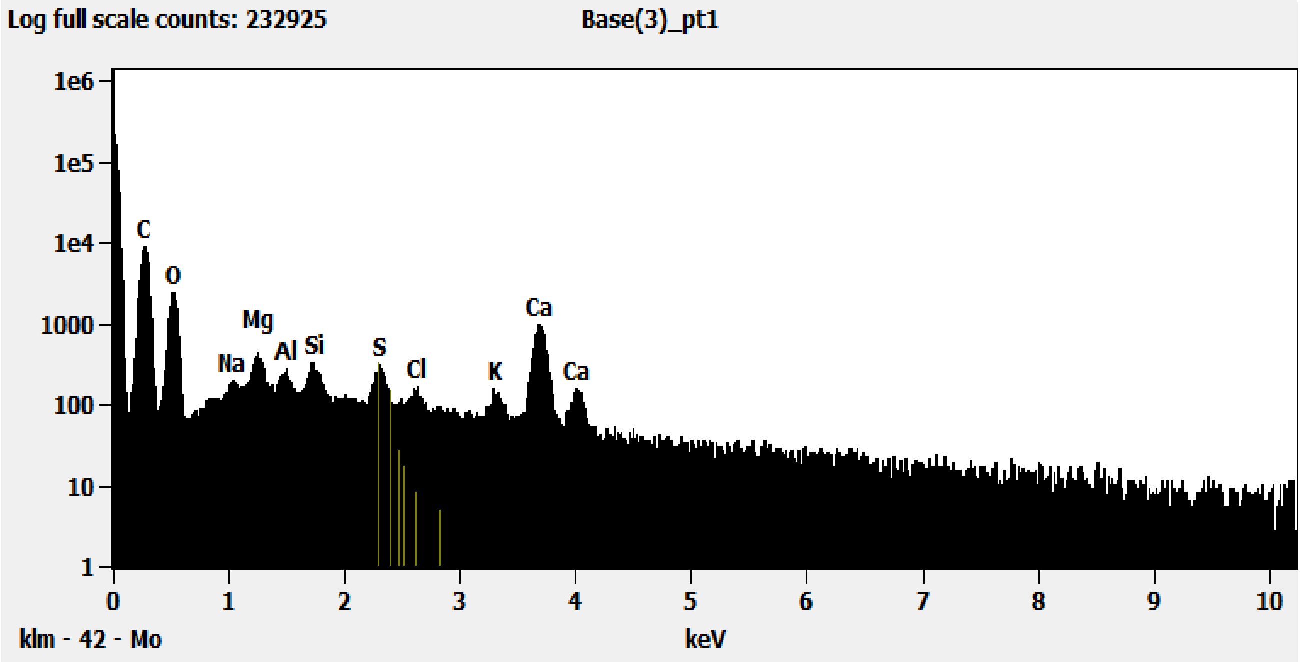

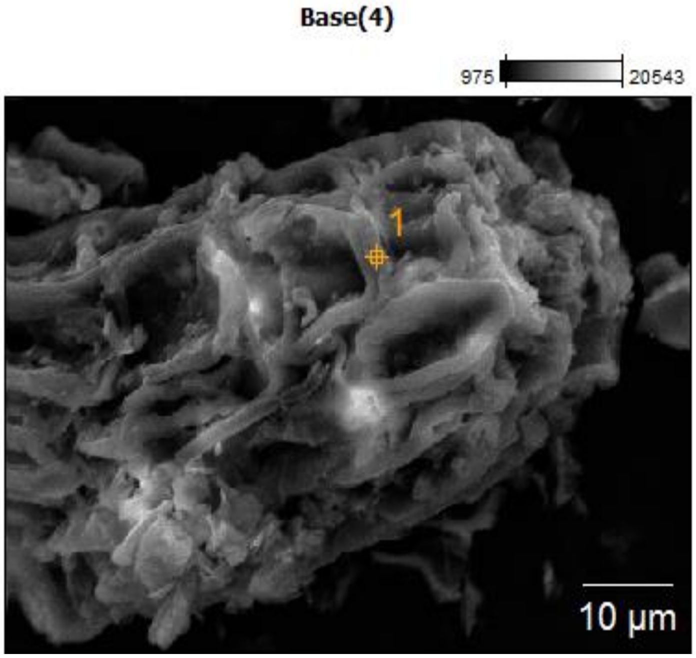

Image Name:	Base(4)
Image Resolution:	512 by 384
Image Pixel Size:	0.15 µm
Acc. Voltage:	15.0 kV
Magnification:	1600

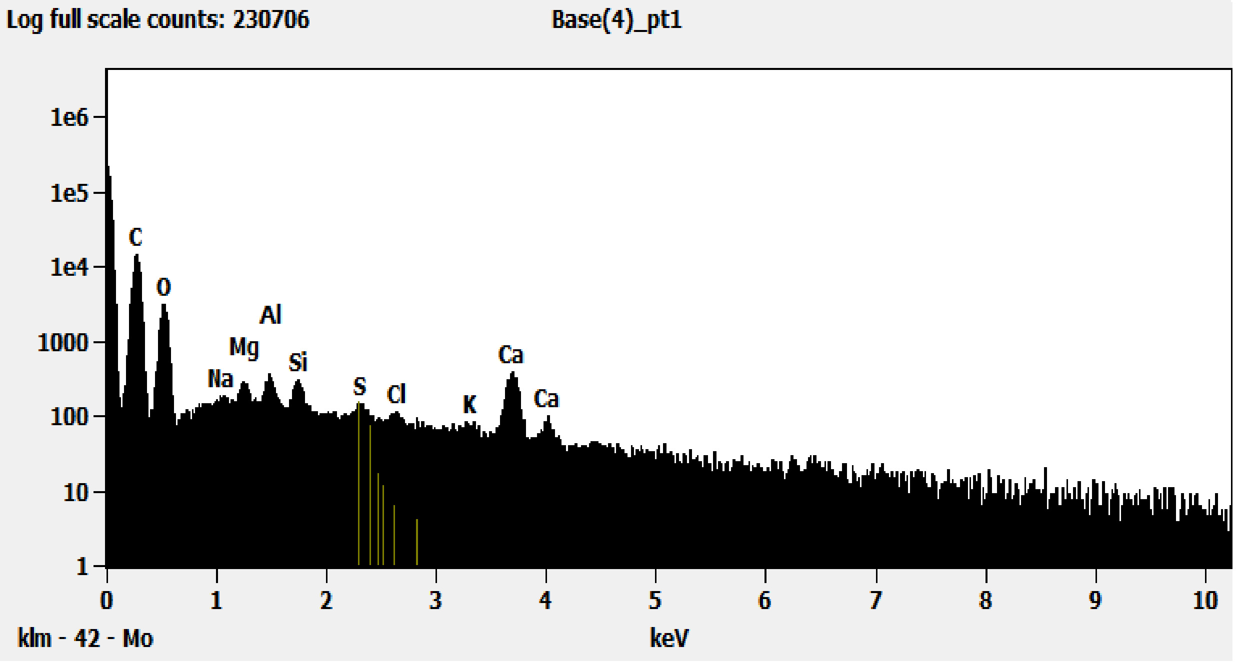

Base(5)

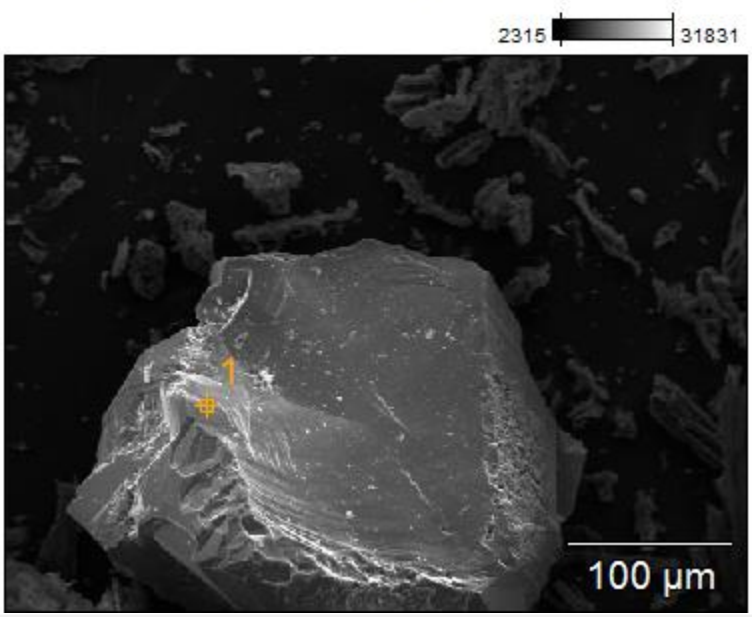

Image Name:	Base(5)
Image Resolution:	512 by 384
Image Pixel Size:	0.88 µm
Acc. Voltage:	15.0 kV
Magnification:	270

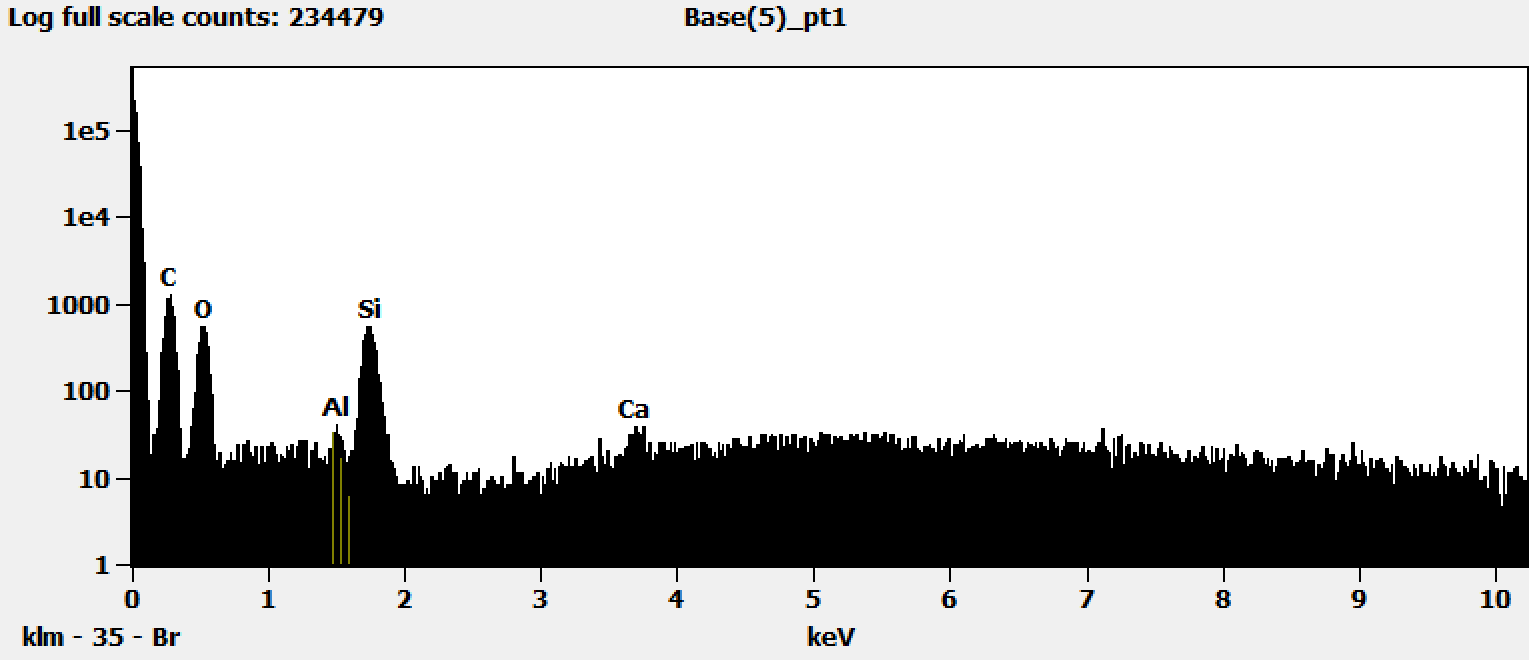

Base(6)

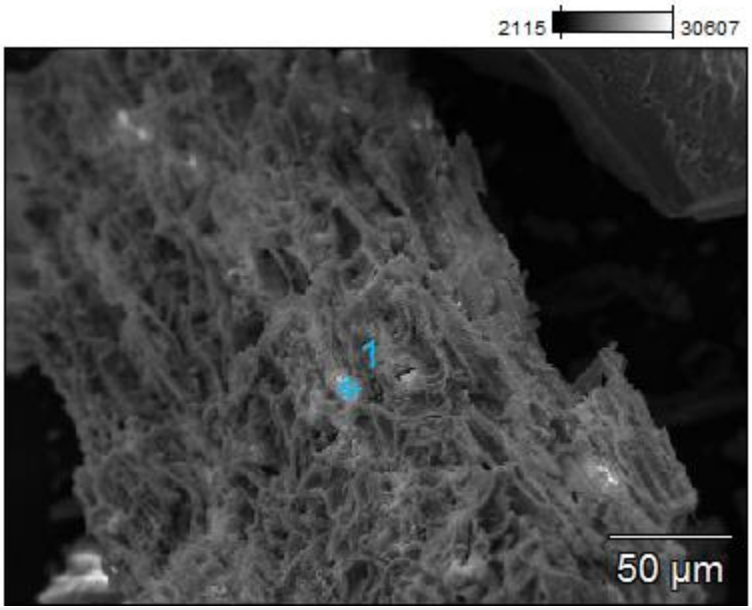

Image Name:	Base(6)
Image Resolution:	512 by 384
Image Pixel Size:	0.59 µm
Acc. Voltage:	15.0 kV
Magnification:	400

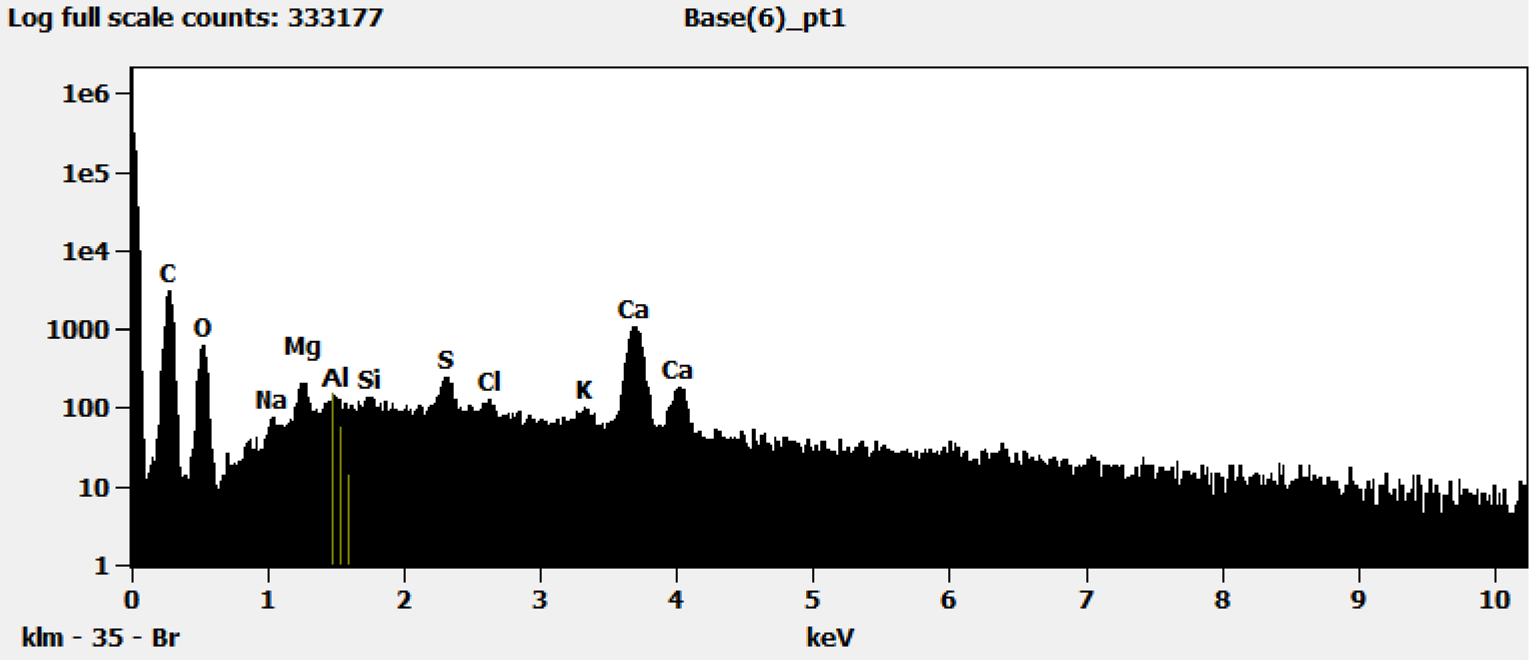

Base(7)

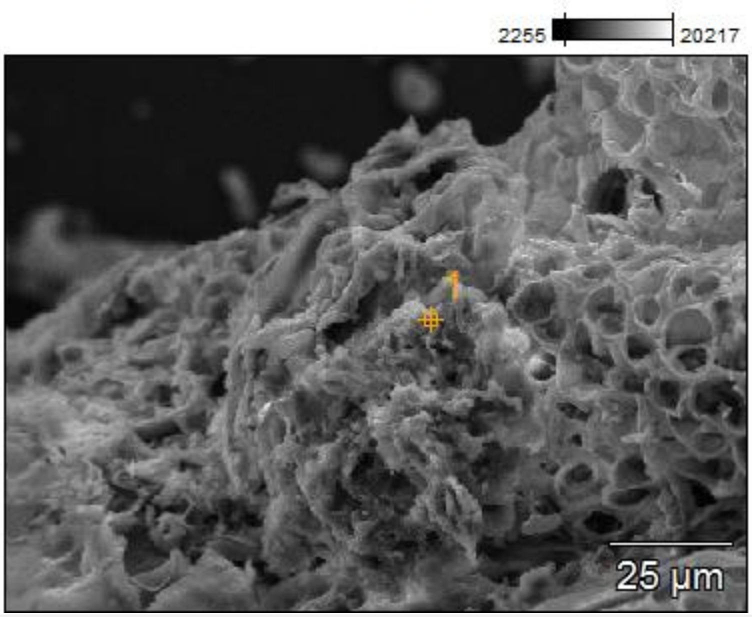

Image Name:	Base(7)
Image Resolution:	512 by 384
Image Pixel Size:	0.30 µm
Acc. Voltage:	15.0 kV
Magnification:	800

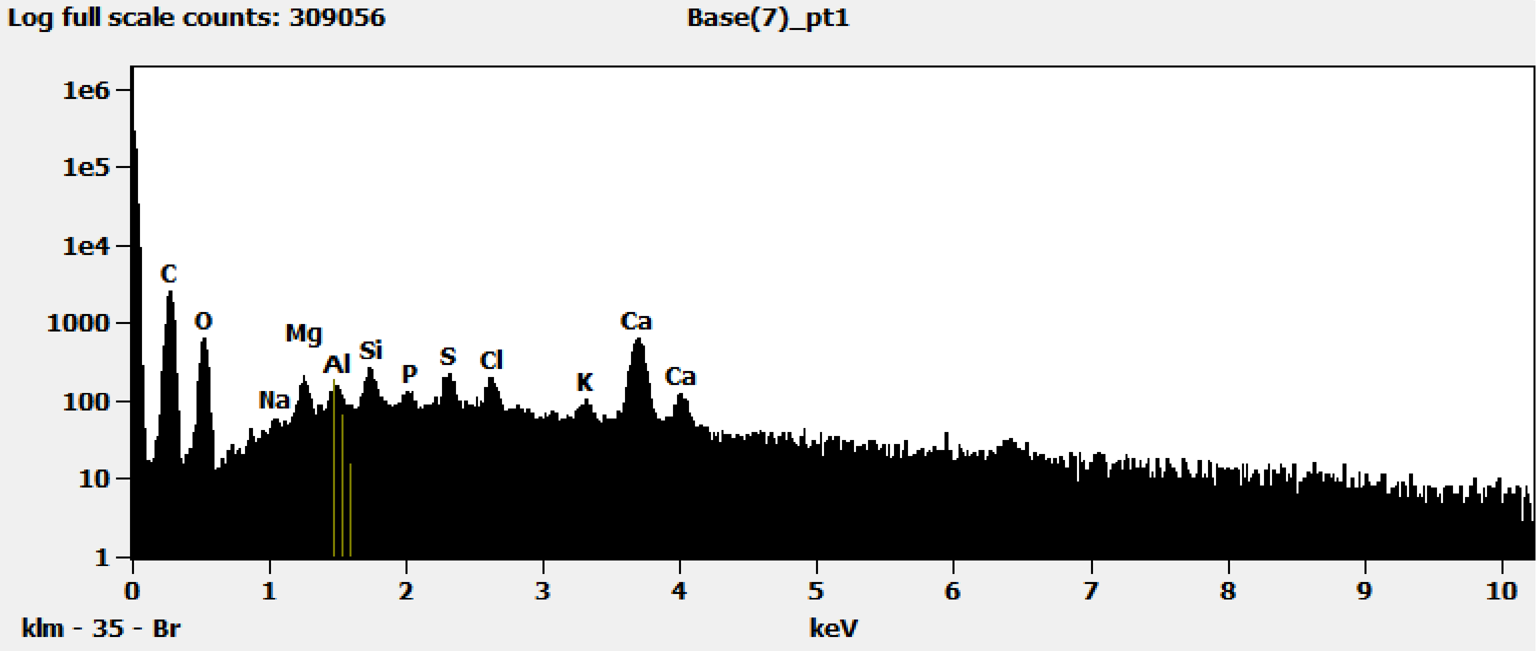

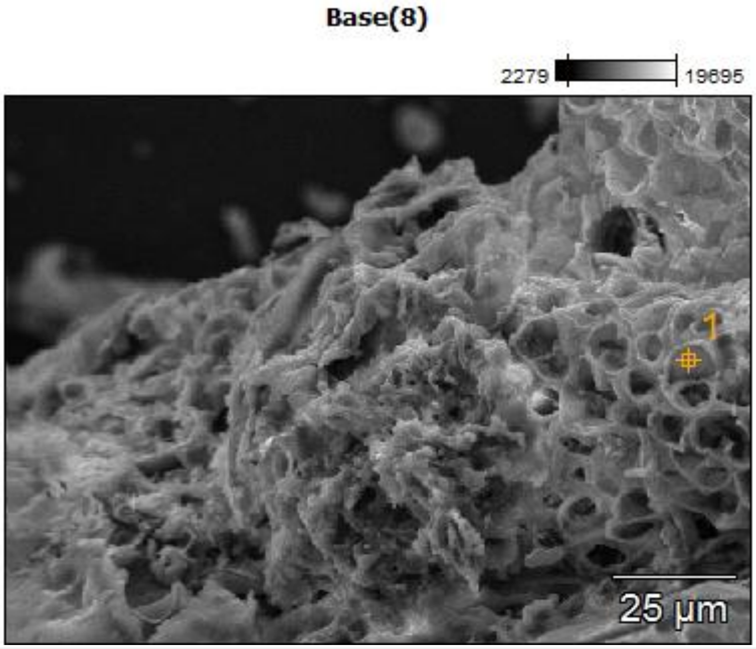

Image Name:	Base(8)
Image Resolution:	512 by 384
Image Pixel Size:	0.30 µm
Acc. Voltage:	15.0 kV
Magnification:	800